Title	Quantum dot solar cell utilizing optical properties of carbon nanotubes
Author(s)	JUNTHORN, Udorn
Citation	高知工科大学, 博士論文.
Date of issue	2017-03
URL	http://hdl.handle.net/10173/1507
Rights	
Text version	ETD

Quantum dot solar cell utilizing optical properties of carbon nanotubes

カーボンナノチューブの光学特性を応用した量子ドット太陽電池

Udorn Junthorn

A DISSERTATION SUBMITTED IN PARTIAL FULFILLMENT
OF THE REQUIREMENTS FOR
THE DOCTOR DEGREE OF PHYLOSOPHY
FACULTY OF GRADUATE SCHOOL
KOCHI UNIVERSITY OF TECHNOLOGY
2017

Dissertation
Entitled

Quantum dot solar cell utilizing optical properties of carbon nanotubes

was submitted to the Faculty of Graduate Studies, Kochi University of Technology
for the degree of Doctor of Engineering (Electronics and Photonic System Engineering)
on 23rd March, 2017

Mr. Udorn Junthorn,
Ph.D. Candidate

Assoc.Prof. Hiroshi Furuta,
Ph.D.(Physics)
Advisor

Prof. Akimitsu Hatta,
Ph.D. (Electrical Engineering)
Co-Advisor

Prof. Chaoyang Li,
Ph.D. (Photonics and Electronics Device Engineering)
Co-Advisor

Prof. Hideo Khono,
Ph.D.
Committee

Assoc. Prof. Hisao Makino,
Ph.D.
Committee

Prof. Akimitsu Hatta,
Ph.D. (Electrical Engineering)

Head of Graduate School

Abstract

In the first part of research, the relationship between the physical structure of carbon nanotube (CNT) honeycomb structures and their total, diffuse, and specular reflectance is investigated for the first time. It is found that CNT honeycomb structures with average cell areas of smaller than 30 μm^2 show a higher total reflectance. Particularly, a thinner, highly packed CNT (buckypaper) film, along with a larger wall height and higher ratio of wall height to cell area, markedly increase the total reflectance for cell areas smaller than 30 μm2, which means that a higher total area of buckypapers in CNT walls and bottom areas increases the total reflectance, including the diffuse reflectance. It is also found that the total reflection of non-absorbed light in CNT honeycomb structures consists primarily of diffuse reflectance.

In the second part of research, Multi-walled carbon nanotube (MWCNT) forests grown on a stainless-steel substrate were used as a photoanode in CdSe/ZnS (core/shell) quantum dot (QD) sensitized solar cells (QDSSCs). QD-treated MWCNTs on the conductive metal stainless substrate showed a higher power conversion efficiency (PCE) of 0.015% than those grown on a doped silicon substrate with a PCE of 0.005% under AM 1.5 sunlight intensity (100 mW/cm^2). This higher efficiency can be attributed to the lower sheet resistance of 0.0045 Ω/sq for the metal substrate than the value of 259 Ω/sq for doped silicon. The relationship between the total reflectance of the as-prepared CNT photoanode and the PCE was investigated for CNTs of various heights and amounts of QDs. A QDSSC fabricated using a CNT photo anode with a height of 25 μm showed the highest efficiency of 0.014 with the lowest total reflectance of 1.9%, which indicates a higher surface area of CNTs and a larger amount of QDs. The as-grown 25-μm CNTs combined with 25 mL of QDs in toluene solutions exhibited the highest PCE of 0.015%, due to the larger surface area of the CNTs and the higher light absorption from the large amount of QDs on the CNTs.

ACKNOWLEDGEMENT

I would like to express my gratitude to a number of people without whom the study would not have been possible.

First of all, I am greatly thankful to Assoc. Prof. Dr. Hiroshi Furuta who is my major advisor for valuable discussions, suggestions, comments and encouragement. I appreciate his guidance and direction throughout the course of my project.

I would like also to thank my co-advisors, Prof. Akimitsu Hatta for useful discussions, comments, and suggestions, this greatly contributed to the success of this thesis, also Prof. Chaoyang Li who gave me some useful suggestions, and Asst. Prof. Dr. Jun Seok Oh provided me comments and suggestions of some technical wettability experiments

I would like also to thank committees, Prof. Hideo Kohno for giving comments at optical reflectance and Assoc. Prof. Hisao Makino for suggesting about solar cells.

I would like to greatly again thank Prof. Chaoyang Li laboratory for kindly supporting solar cell fabrication and some useful comments and suggestions.

I would also like to thank Mr. Shengwen Hou from Prof. Li laboratory for solar cell preparation and some information about this experimental method

This acknowledgement is also extended to Department of Photonics System and Electronics Engineering, Faculty of System Engineering, Kochi University of Technology (KUT), Japan for the access to all facilities related to our research and the Special Scholarship Program (SSP) and Japanese Government scholarship (MEXT) for financial support in part, also special thanks to International Relation Division (IRD) for all research-assisted supports and suggestions how to happily live in Japan as a foreign student. This PhD dissertation would not be complete without a partially financial support from Thai-Nichi Institute of Technology (TNI), Thailand.

Finally, the greatest appreciation must be given to my parents, brother, sister, sister-in-law, lovely nephews and nieces and Thai best friends, in particularly for those who was happily working together, Adam san, Mamun san, Vlado san, Koji san, Sekiya san, Kusumoto san, Ishimoto san, Tanami san, Shoko san, Hongo san, Miyaji san, and Hayashi san in Hatta and Furuta Laborlatory, Thai community in Kochi prefecture, good colleagues at TNI for all their support and spiritual encouragement for my success. I also would like to thank other people who helped me in one way or another.

Udorn Junthorn

March 2017

DEDICATION

The author wishes to dedicate this desecration to his family and teachers

List of Tables

List of Figures of Chapter 1

Lists of Figures (Continued)

List of Figures of Chapter 2

Lists of Figures (Continued)

Lists of Figures of Chapter 3

TABLE OF CONTENTS

CHAPTER 1

Objectives, Abstract of Dissertation, Research background, CNT synthesis and Characterization

1.1 A structure of this dissertation

Chapter 1: Objectives, abstract of dissertation, and research background

Part I: Carbon nanotubes (CNTs)

Part II: Quantum dots (QDs)

Part III: Carbon nanotubes and quantum dots in solar cells

Part IV: CNT synthesis and data characterization

Chapter 2: Part I of research work: Carbon Nanotube (CNT) Honeycomb Cell Area-Dependent Optical Reflectance

Chapter 3: Part II of research work: CdSe/ZnS quantum dot (QD) sensitized solar cell utilizing a multi-walled carbon nanotube photoanode on stainless steel substrates

Chapter 4: Conclusion of overall research

1.2 Objectives

In this dissertation, my works focused on an application of CNTs to improve an efficiency of quantum dot solar cells (QDSSCs). In this research, originality ideas were provided as follows:

1) In order to utilize the reflected light of CNT structures for QDSSCs, total, diffuse, and specular optical reflectance of carbon nanotube (CNT) honeycomb structures was investigated. (published paper in Nanomaterials)
2) To investigate efficiencies improvement by the utilization of optical reflectance to improve the quantum dot sensitized solar cell (QDSSCs) efficiency, and to investigate CNT forests grown on stainless steel serving as a photoanode for CdSe/ZnS core/shell QDSSCs as a means of reducing the resistivity to improve photovoltaic efficiency (submitted to International Journal of Electrochemical Science)

1.3 Abstract of Dissertation

This dissertation focuses on an application of CNTs to improve an efficiency of quantum dot solar cells (QDSSCs) utilizing optical reflectance carbon nanotubes. The originality ideas were provided firstly to utilize the reflected light, total, diffuse, and specular optical reflectance of carbon nanotube (CNT) honeycomb structures. Secondly, the novel study is to investigate efficiencies improvement by the utilization of optical reflectance to improve the quantum dot sensitized solar cell (QDSSCs) efficiency, and to investigate CNT forests grown on stainless steel serving as a photoanode for CdSe/ZnS core/shell QDSSCs as a means of reducing the resistivity to improve photovoltaic efficiency.

The unique morphologies and structures of carbon nanotubes (CNTs) have received much attention for optical and electronic applications because CNTs have extraordinary photonic properties, high electrical current endurability, and mechanical stiffness. In addition, the morphologies of CNT forests can be modified to enhance charge generation, separation, and transport in optical-electronic applications. For modifying CNT forest morphologies, liquid or vapor treatment is a simple, economic method that provides a high yield. The liquid treatment of CNTs exhibits self-assembly, where one-dimensional material forms into three-dimensional micro or macro structures with various morphologies. The liquid and vapor treatment onto multi-walled CNTs (MWCNTs) exhibits the self-assembly of hierarchical networks to form honeycomb structures due to capillary forces arising during solution evaporation. The larger surface area of such honeycomb structures is expected to allow the efficient assembly of sensitized nanoparticles of quantum dots (QDs), which can serve as an electrode scaffold to capture and transport photo-generated electrons in solar cells. Additionally, the spacing in the structure of silicon solar cells with CNT honeycomb top electrodes allows higher transmission of light to photo-active parts of solar cells when light irradiation is perpendicular to the substrate. Moreover, wall-shaped condensed CNT films can serve as an “electron-carrying highway”, enhancing high conductivity to an electrode of solar cells. The total reflectance of randomly oriented CNT-compressed sheets is more than 80% for a CNT film thicknesses of 0.3–1 μm, while for high nanotube forests (300–500 μm in height) it is 1%–2% across a range from UV to mid IR (200–2000 nm). Yang et al. reported an extraordinarily low total reflectance

of 0.045% for a mat of vertically aligned multi-walled carbon nanotubes (VA-MWCNTs) forests in a visible region at wavelengths of 457–633 nm. Theoretically, the reflectance of CNT forests can be explained by the fact that, for light incidence on a forest top surface of CNTs of small angle with respect to the CNT axis, electrons on the CNT body cannot couple with the electric fields, which provides a weak optical interaction between the CNT forests and normally incident light resulting in a lower total reflectance.

For photovoltaic applications, the optical properties of the materials are one of the most important parameters for achieving light enhancement. Recently, the reuse of the optical reflectance of existing light to significantly increase the efficiency in dye sensitized solar cells (DSSC) has been reported. It is expected that solar cells using CNTs can be designed so that the highly-reflected light from the CNTs is absorbed by sensitizers, generating a larger number of electron-hole pairs.

In the first part, the aims are to study the relationship between the physical structure of CNT honeycomb structures and the total, diffuse, and specular reflectance of the CNT honeycomb structures. It can be summarized that this study investigated the controlling of cell area in a CNT honeycomb structure by a simple method of ethanol treatment, in which the average cell area could be decreased by a shorter evaporation time of ethanol. The total, diffuse, and specular reflectance of CNT honeycomb structures was investigated. Cell areas smaller than 30 μm2 with a 3–8 μm wall height showed a higher total reflectance of 6%–12% in the UV region and 6%–8% in the visible region, where as-synthesized CNT forests exhibited corresponding values of 0.5% and 1.0% in the UV and visible regions, respectively. In particular, our findings highlighted that thinner buckypaper films of high-density CNTs in cooperation with a higher ratio of wall height to cell area (larger surface area) and wall height increases the total and specular reflectance. In addition, we found that the highest measured diffuse reflectance of 11% in the UV region, as well as the total reflectance, is likely strongly influenced by a higher total area of buckypapers in CNT walls and bottom areas. Interestingly, this study found that the main component of total reflectance from CNT honeycomb structures is diffuse reflectance. In the next part, it is expected that a total reflectance will be obtained for

larger surface areas, which will contribute to the achievement of efficient absorption of light into quantum dots to improve the efficiency of QD solar cells utilizing CNT electrodes.

In the second part, the aims are to study the utilization of optical reflectance to improve the quantum dot sensitized solar cell (QDSSCs) efficiency, and to investigate CNT forests grown on stainless steel serving as a photoanode for CdSe/ZnS core/shell QDSSCs as a means of also improving photovoltaic efficiency. As mentioned in the first part, the extraordinary mechanical, chemical, and electronic properties of carbon nanotubes (CNTs) make them outstanding materials for energy applications. The modified CNT structure is expected to be a good material for use as a counter electrode or photoanode with semiconducting quantum dots (QDs) in order to harvest a broader range of light from the ultraviolet (UV) to the infrared (IR). A significant increase in optical total reflectance using a structural modification of CNT honeycombs, which will increase the utility of CNT honeycomb structures in high-efficiency solar cells. QD-decorated CNTs exhibit efficient charge transfer from photoexcited QDs to the CNTs. QD sensitized solar cells (QDSSCs) have attracted considerable interest from researchers because their power conversion efficiency (PCE) may exceed the Shockley and Queisser limits. In particular, QDs can harvest a broad range of optical wavelengths by multiple exciton generation (MEG), thus improving the photovoltaic efficiency. Optical absorption by QDs fabricated from materials such as CdS, CdSe, and CdSe/ZnS is intrinsically tunable from the UV to the near-IR due to the particle-size dependence of the bandgap. A major advantage of QDs as light sensitizers compared with conventional dyes is that electron recombination is suppressed, thereby improving the efficiency of QDSSCs. One dimensional (1D) wires, of e.g., TiO_2, ZnO, and Si have been extensively used for electron transfer from QDs to electrodes. In particular, CNTs have arisen as a superior candidate 1D wire electrode material for QDSSC because of their large surface area, high conductivity, high aspect ratio, and chemical stability. Due to their excellent electrical and thermal conductivity, flexible metal substrates serving as a counter-electrode of DSSCs can reduce both the sheet resistance and production cost of solar cells. It was reported the PCE of QDs/Si coaxial nanowires on the gold (Au) sputtering metal electrodes in QDSSCs shows 0.253%.

From this the study, it was found that Multi-walled carbon nanotube (MWCNT) forests grown on a stainless-steel substrate were used as a photoanode in CdSe/ZnS (core/shell) quantum dot (QD) sensitized solar cells (QDSSCs). QD-treated MWCNTs on the conductive metal stainless substrate showed a higher power conversion efficiency (PCE) of 0.015% than those grown on a doped silicon substrate with a PCE of 0.005% under AM 1.5 sunlight intensity (100 mW/cm2). This higher efficiency can be attributed to the lower sheet resistance of 0.0045 Ω/sq for the metal substrate than the value of 259 Ω/sq for doped silicon. The relationship between the total reflectance of the as-prepared CNT photoanode and the PCE was investigated for CNTs of various heights and amounts of QDs. A QDSSC fabricated using a CNT photo anode with a height of 25 μm showed the highest efficiency of 0.014% with the lowest total reflectance of 1.9%, which indicates a higher surface area of CNTs and a larger amount of QDs. The as-grown 25-μm CNTs combined with 25 mL of QDs in toluene solutions exhibited the highest PCE of 0.015%, due to the larger surface area of the CNTs and the higher light absorption from the large amount of QDs on the CNTs.

In conclusion, firstly the relationship between CNT honeycomb structures and the total, specular, and diffuse reflectance was investigated. CNT honeycomb structures with average cell areas of smaller than 30 μm^2 show a higher total reflectance. Secondly, the first QDSSCs with photoanodes of MWCNTs on a metal substrate, and found that the PCE for such QDSSCs on stainless steel substrates was three times higher than those on a low-resistivity (0.15 Ω·cm), doped silicon substrate. Also, the lower total reflectance QD-treated CNT forest of 25-μm height achieved a higher PCE. The as-grown 25-μm CNTs combined with 25 mL of QDs solutions exhibited the better PCE.

1.4 Carbon nanotubes (CNTs)

Carbon nanoutbes (CNTs) were found by Sumio Ligima in 1991 [1]. CNTs have a cylindrical structure with allotrope carbon. CNTs can be rolled up into a tube shape by one atomic layer of graphene sheet as single-walled carbon nanotubes (SWCNTs) and multi-layers of graphene sheets as multi-walled carbon nanotubes (MWCNTs). CNTs have a very high ratio surface area (tube length-to-width: 28,000,000:1). Due to CNTs consisting of graphitic layers, the sp^2 bonding of graphite are more strength than sp^3 bonding in the other kind of carbon like diamonds. Also, CNTs can be formed as armchair, zigzag, and chiral tubes due to a unit vector of graphene crystal lattice as shown in Fig. 1.1. In this research, MWCNTs were chosen as charge carriers of a photoanode in solar cells since MWNTs provide basically metal or semimetal properties due to the larger CNT tube diameters.

1.4.1 Multi-walled carbon nanotubes (MWCNTs)

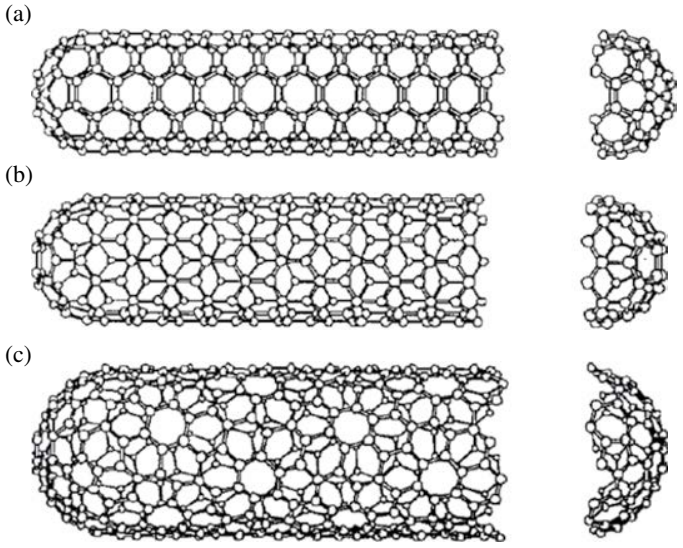

Fig. 1.1 Carbon nanotubes (CNTs) can be formed as (a) armchair tubes (b) zigzagag (c) chiral tubes. Reprinted from [2] with permission from Elsevier.

1.4.2 CNTs synthesis by Chemical Vapor Deposition (CVD)

A chemical vapor deposition (CVD), which a hydrocarbon gas reacts with catalytically metal nanoparticles, is able to grow CNTs. Here, nanoparticles as a catalyst nucleate site initiation of CNT growth. The CVD process can produce CNTs as a large scale. A reaction of the metal nanoparticles such as Fe, Ni etc. and a carbon source of hydrocarbon gases such as CH_4, C_2H_4, and C_2H_2 and carrying gases such as He, Ar etc. with a temperature of up to 1000°C can synthesize CNTs.

1.4.2.1 (I) Hot-filament Chemical Vapor Deposition

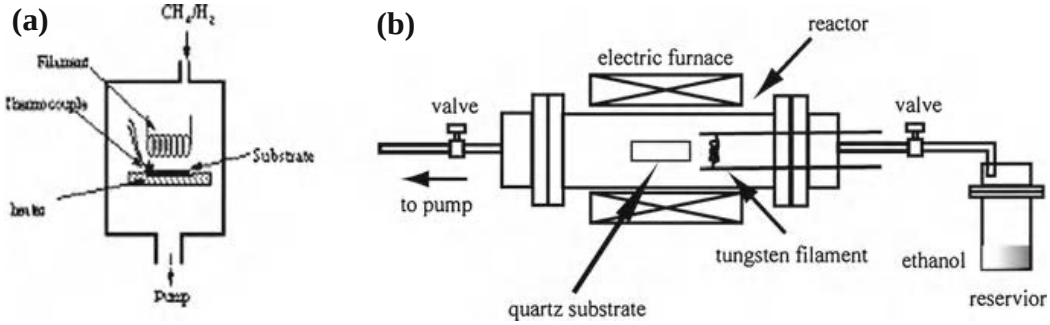

Fig. 1.2 Hot-wire thermal CVD experimental setup. (a) Hot-filament CVD without an external heater. (b) Hot-filament CVD with a furnace heater. Reprinted from [3] with permission from IOPScience.

In the hot-filament CVD without heater, the gas activation required for CVD is achieved by heating a tungsten filament typically up to 2,200 °C. CNTs can be directly deposited on the surface of substrates (Fig. 1.2a). Usually, the thermal irradiation of filament heats a substrate. In a hot-filament CVD with a heater as shown in Fig. 1.2(b), an electric furnace heats the substrate and the substrate temperature is independently controlled using an external heater. The distance between the filament and the substrate, a crucial parameter, can be adjusted from a few millimeters to a few centimeters to produce CNTs.

1.4.2.2 (II) Thermal CVD Growth Mechanisms of CNTs

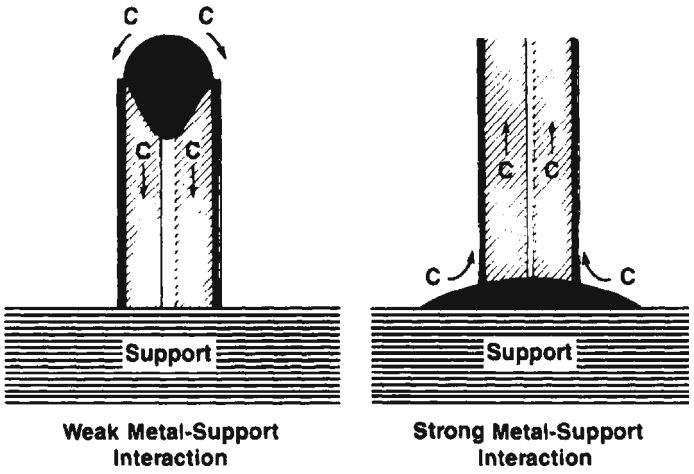

Fig. 1.3 Interaction of metal catalysts support for CNT growth. Reprinted from [4] with permission from Elsevier.

In a mechanism of CNT growth, Nickel, cobalt, stainless steel, gold, platinum, and though tungsten has been used as the catalyst to synthesize CNTs. The growth of CNTs in the thermal CVD can be explained in three main steps which are as follows;

(1) the decomposition of gas molecules of carbon;

(2) the resultant carbon atoms were diffused through the catalysts due to the gradient concentration; and

(3) for a precipitation process of carbon atoms at the nanoparticle interface, in a deposition mechanism, CNTs can be grown catalytically and then thicken via catalyst-free pyrolytic carbon. The nanoparticle catalysts become liquid droplets at the proper high temperature due to vapor–liquid–solid process in the thermal CVD. These catalytic droplets receive carbon atoms from vapor until the saturation state. The carbon precipitation as droplets can grow CNTs. Droplet catalysts are increased from the growth of CNTs in Fig. 1.3(a). The CNTs can be grown where CNTs beneath to the substrate area in Fig. 1.3(b). So, the droplets are formed to be a tube-like at the top of the CNTs due to the gravity droplets of lifting up catalysts.

1.5 Quantum Dots (QDs)

1.5.1 Background of quantum dots (QDs)

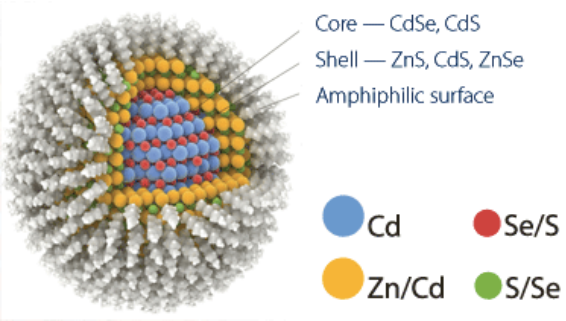

Fig. 1.4 Schematic of core/shell quantum dots. Reprinted from http://en.rusnano.com/

Quantum dots (QDs) as colloidal semiconducting crystallites. QDs are able to generate three electrons by a single incident photon where conventional single crystalline layer semiconductors can generate one electron. When the photon energy eight-time higher than the QDs bandgap energy, QDs can generate seven electrons regarding the Auger recombination inversion. QDs are attractive nanomaterials in photonics and biomedical applications.

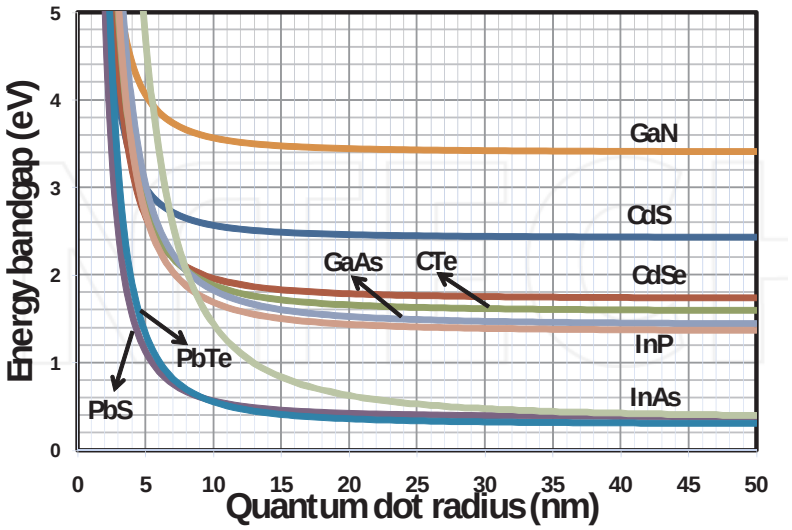

Fig. 1.5 Quantum dot energy bandgap vs. sizes for semiconducting nanomaterials. Reprinted from [5] with permission from InTech.

1.5.2 Properties of QDs

Various examples of quantum dot radius as a function of energy bandgap are exhibited in Fig. 1.5. Multiple exciton generation (MEG) in semiconductoring quantum dots was found by Nozik *et al* [6] in which one photon energy higher than the quantum dot bandgap energy can generate electron-hole pairs. In bulk semiconducting materials, the photon energy higher than their bandgap energy can be absorbed to create the electron where a group of electrons are called hot carriers as shown in Fig.1.6(a). Before reaching the bottom of the conduction band, the excited electron undergoes many multi-phonon emission before the excite electrons approach in the bottom of conduction band. In a contrary, an impact ionization process (carrier multiplication) is undergone by the hot carrier in a quantum dot. Therefore, a single photon can generate multiple electron-hole pairs (MEG). Thus, the UV spectra with higher photon energy can create more electrons than near infrared spectra. Figure 1.6(b) schematizes timing process of MEG after charge carriers are excited [7]. The impact ionization takes hot carriers 0.1 ps, then the cool down will take 2 ps later. The Auger recombination will take 20 ps, and the cool down system will take 2 ps before a new excitation. The transient absorption spectroscopy can quantify to investigate MEG process via the impact ionization or Auger recombination inversion.

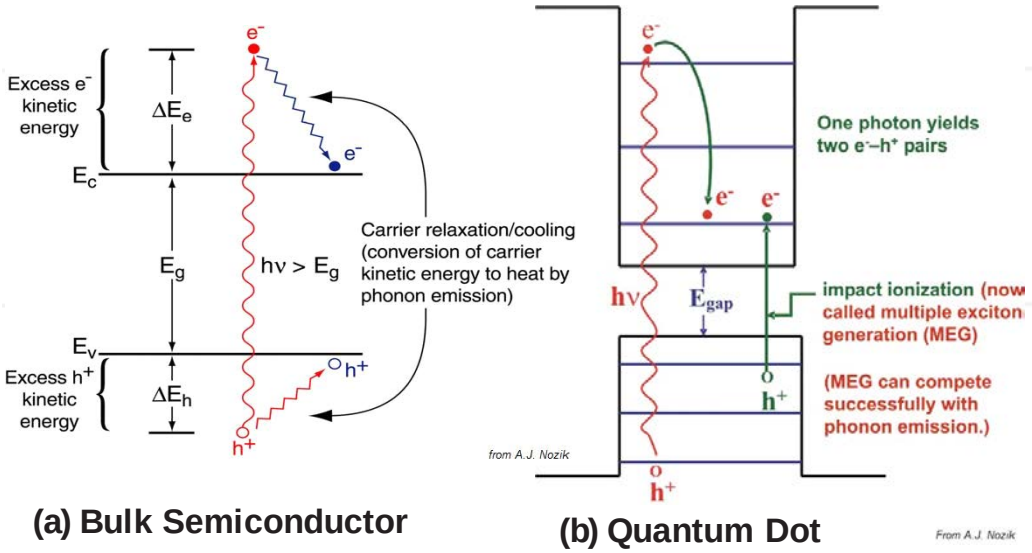

Fig. 1.6 Comparison of hot carriers thermalization in (a) a bulk semiconductor and (b) a quantum dot. Reprinted from [16] with permission from American Chemical Society.

1.6 Carbon nanotubes (CNTs) and quantum dots (QDs) in solar cells

1.6.1 Carbon nanotubes (CNTs) and QDs in photovoltaics

According to CNT outstanding electrical and optical properties, CNTs have been utilized in photovoltaic applications as charge (electrons) carriers. Also, QDs have been revealed as a photo-sensitizer. A utilization of CNTs can be a key to a QD limitation. CNTs as nanotubes can not only directly promote charge transport, but also efficiently support electrons from QDs to improve the solar cell performance.

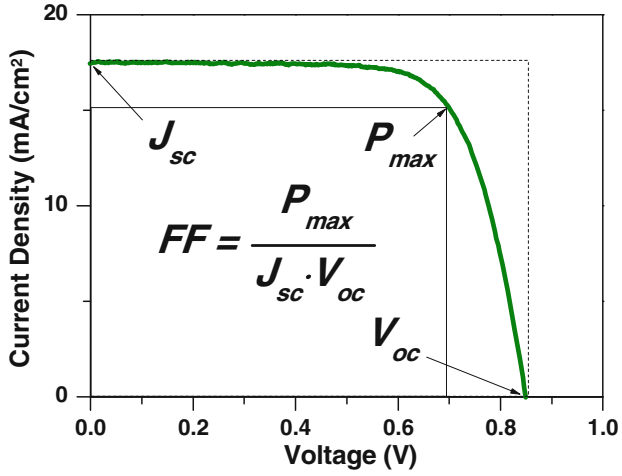

Fig. 1.7 Current density-voltage characteristics (J-V curve). Reprinted from [9] with permission from Springer.

In solar cell efficiency analysis, three important parameters: a short-circuit current (I_{sc}), an open-circuit voltage (V_{oc}), and a fill factor (FF) have influential to the power conversion efficiency (PCE) of solar cells. The fill factor (FF) is conversely proportional to V_{oc} and I_{sc}. Therefore, key factors to determine PCE are V_{oc} and I_{sc}. A photon energy higher than material's bandgap energy will generate an electron carrying into an external circuit. The fill factor (FF) can be calculated from the maximum area of *I-V* or *J-V* curves as shown in Fig. 1.7 under a light incidence as an expression below

$$FF = \frac{V_m I_m}{V_{OC} I_{sc}}$$

where V_m and I_m are the maximum voltage and max current, respectively. In this case, the efficiency of energy conversion is provided by:

$$\eta = \frac{V_{OC} I_{SC} FF}{P_{in}}$$

where P_{in} is the input power.

1.6.2 Dye sensitized solar cells (DSSCs) vs. Quantum dot sensitized solar cells (QDSSCs)

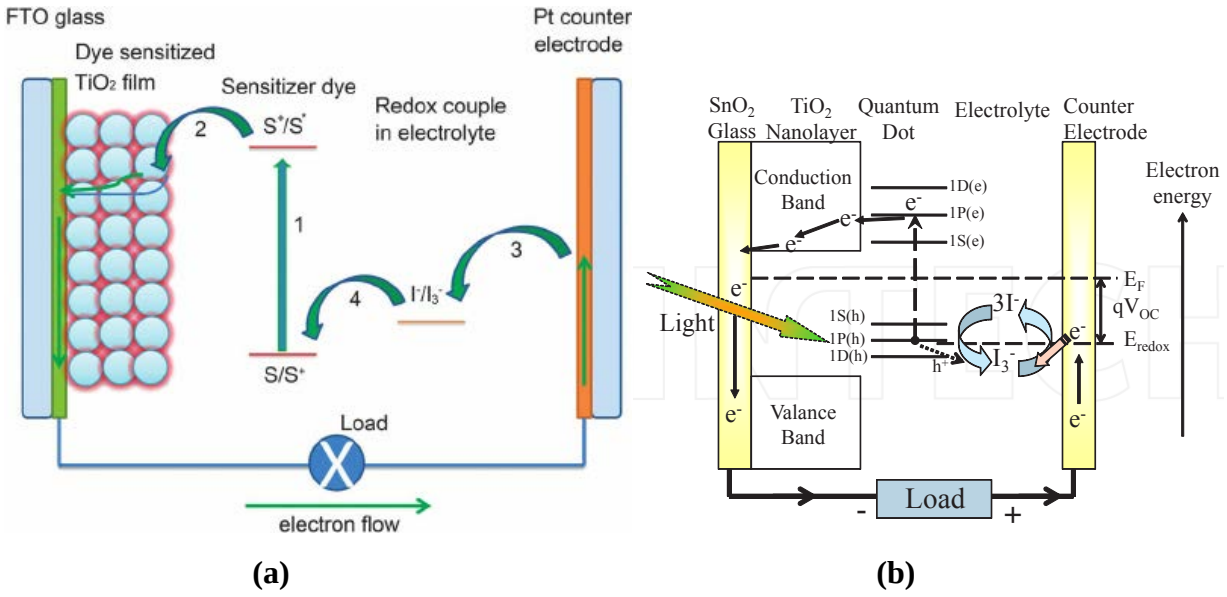

(a) **(b)**

Fig. 1.8 Schematic diagram illustrating the structure and operation of (a) Dye-sensitized solar cells (DSSCs), quantum dots-sensitized solar cell (QDSSCs. Reprinted from [5] with permission from InTech.

In conventional DSSCs, as can schematized in Fig. 1.8(a) the light is incident into the transparent electrode through the dye photo-sensitizer. Photon energy excite electrons from the valence band to the conduction band then flow into the titanium dioxide (TiO_2). The electrons transport into the conductive transparent electrode where they are collected passing through a power load. The electrons transport to re-introduced into on a metal counter electrode (CE) on the back of the cell, moving into the electrolyte as a re-dox reaction. Finally, the electrons flow back to the dye molecules. TiO_2 have been mainly employed as an electrode due to a high efficiency. There is a main problem in obtaining the higher photo-conversion efficiency according to a transport of electrons across the oxide particle network. Additionally, due to many boundaries on a random path of the electrons, the recombination is possible with oxidized photo-sensitizers,

before efficiently transporting to the electrode part. Therefore, quantum dots can be utilized in many kinds of solar cells: 1) metal-semiconducting junction [10], 2) polymer-semiconductors, and 3) semiconductor-semiconductors. QDs attached to n-C60 composite clusters [11], or single and multi-walled CNTs based solar cells [12], [13].

As mentioned eelier, instead of using dye in a dye sensitized solar cells, quantum dots are utilized as a photo receiver to generate charge carriers [5], [14], [15]. One of the advantages of QDs, QDs can be produced in situ or more from a colloidal QD solution. A suitable bandgap of QD sensitizer should match to increase electron injections into conduction band of TiO_2 thin film. CdS, CdSe, and CdTe QDs as sensitizers have been focused as QD synthesized solar cells focused on [16]–[18]. Figure 1.8(b) shows an illustrating schematic of photovoltaic cell. It consists of four main components: photoanode, countercathode part, nanostructure TiO_2 layer, QDs energy levels, and electrolytes solution. The counter electrode is usually coated with catalysts of platinum or graphite.

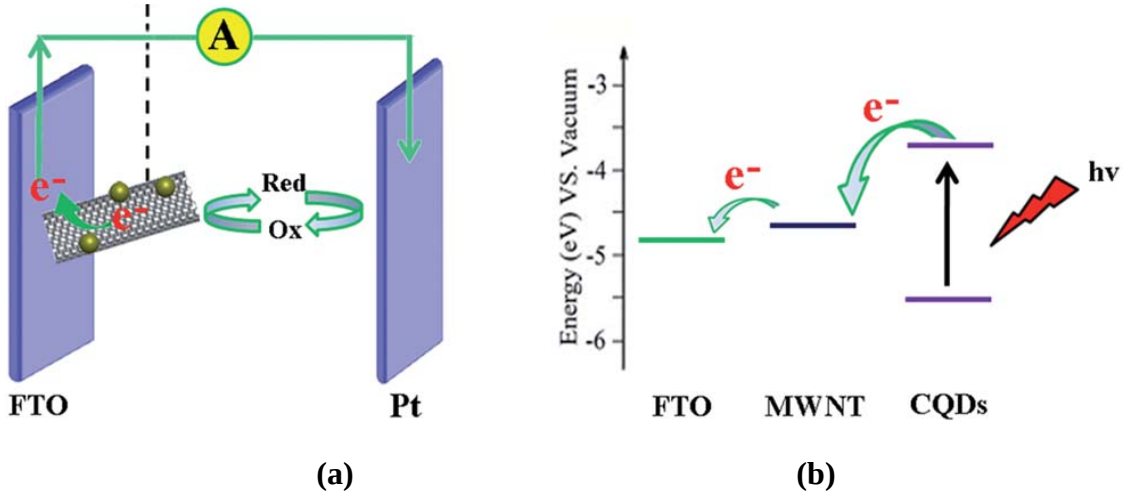

Fig. 1.9 (a) Schematic of CNTs in QDSSCs (b) Energy bandgap levels of QDs and MWCNTs. Reprinted from [19] with permission from RSC Advances.

A gap of the problems is inconvenient enlarging of oxide electrode surface area. Hence, an ability of electron-accepting of semiconducting CNTs could be served as the pathway directly to flow photogenerated electrons as shown in Fig. 1.9(a). Therefore, CNTs can be served as a pathway of carrying charges for the electrode surface in DSSCs or QDSSCs in which CNTs can be used as anchor light harvesting semiconducting QD particles. In our research, due to a low-cost

production and relatively high efficiency of dye sensitized solar cells (DSSCs), quantum dot can replace dye due to a low electron recombination, adsorbed onto larger band gap metal oxide nanoparticles, intrinsically strong light absorption, and large surface areas.

1.7 Synthesis of Carbon nanotubes (CNTs)

1.7.1 Direct Current (DC) magnetron/radio frequency (RF) magnetron sputtering equipment

A sputtering system is described that energetic ions from the plasma of a bombard of gaseous discharge to a target called a discharge cathode. With a collision of energetic ions from the gaseous discharges, the anode (substrate) can be coated from the ejected target atoms [20]. The direct current (DC) sputtering equipment shown in Fig. 1.10(a) utilizes a DC gaseous discharge, ions collide the target to be deposition source. The substrate is the anode with the power supply of a high-voltage DC., the target and substrate with a capacitor as can be seen in Fig. 10(b) in the radio frequency (RF) sputtering) as shown in Fig. 1.10(b). The capacitor is partially to support of an impedance-matching network that proves the voltage from the RF source to discharge the plasma. The process of RF-sputtering offers, in particular, sputtering of an electrically insulating target become possible over DC sputtering method. The magnetron sputtering is the rare sources of a high sputtering deposition. As the magnetron is a magnetically assisted discharge, in the DC and RF sputtering process with a perpendicular electric field. Magnetic flex parallel to the surface of the target can be generated by the Magnetron configuration serving as a permanent magnet. The magnetic field controls the plasma in the chamber space over the target in order to trap electrons near the target surface [21]. In our research, CNT catalysts were deposited by both DC and RF magnetron sputtering systems. Sputtering conditions were provided in Chapters 2 and 3 in different acquisitions.

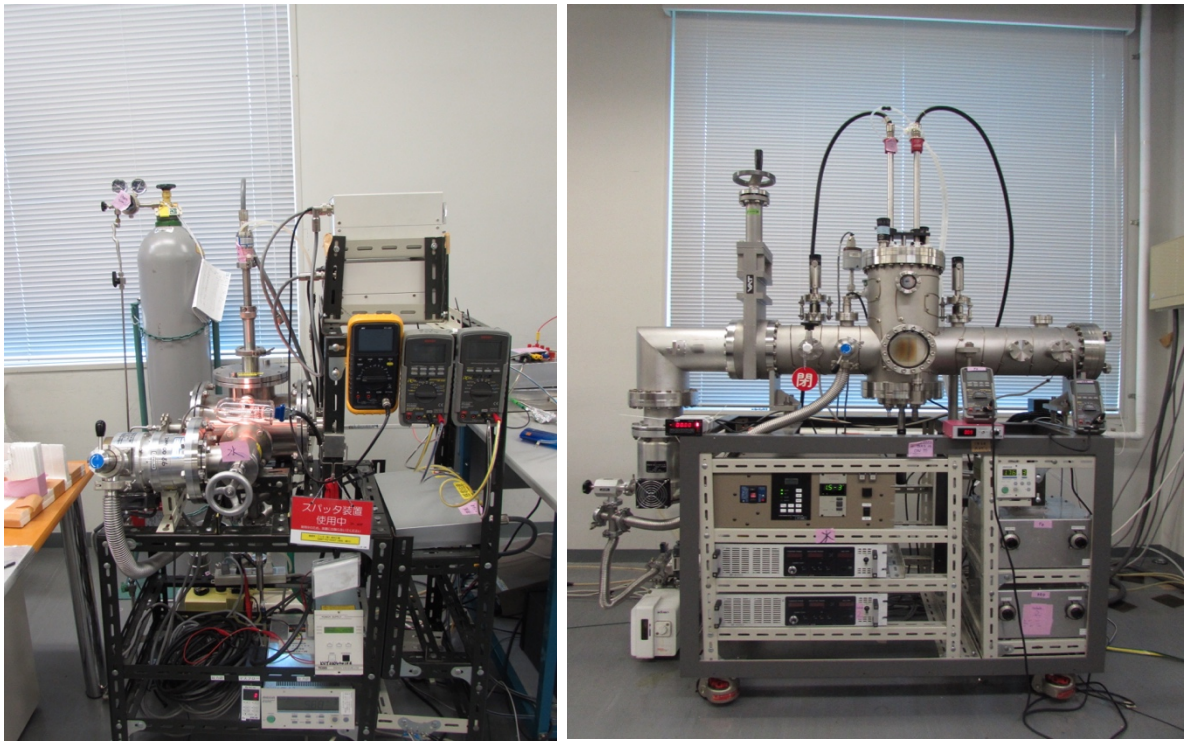

(a) **(b)**

Fig. 1.10 (a) DC magnetron sputtering equipment, (b) RF magnetron sputtering equipment in our laboratory.

1.7.2 Thermal Chemical Vapor Deposition (CVD)

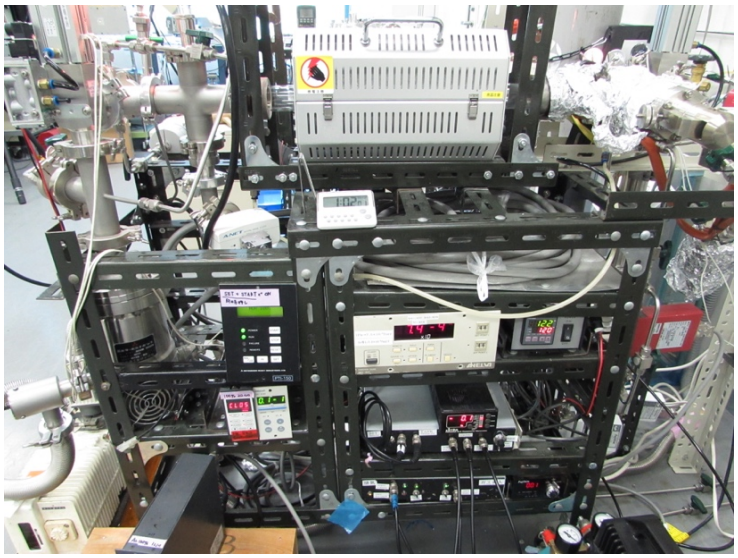

Fig. 1.11 Thermal-CVD equipment in our laboratory

As mentioned earlier regarding the CVD process, the hot-filament (thermal) CVD in our laboratory is capable to grow a high quality of CNTs as acquisitions, detailed in Chapters 2,3. Field-emission SEM images of CNT samples which were deposited in our laboratory as displayed in Fig. 1.12.

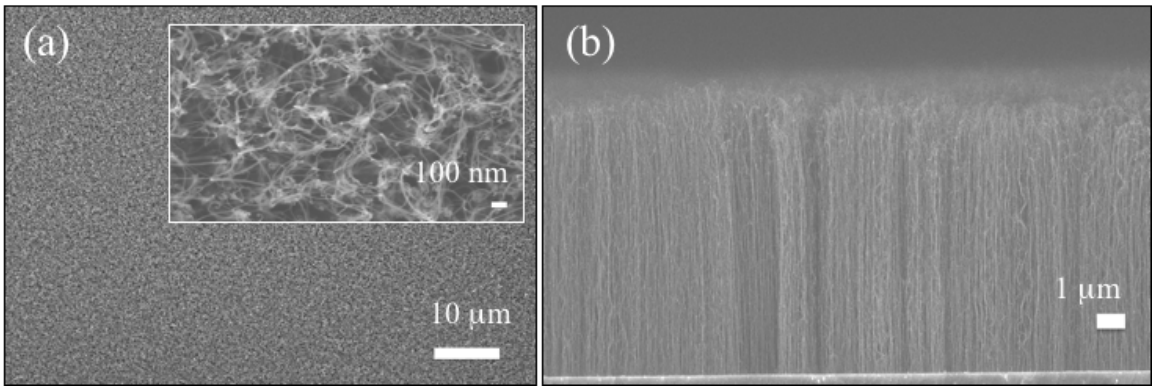

Fig. 1.12 FE-SEM images of CNTs grown on a silicon substrate deposited by a Fe/AlOx catalysts in the hot-filament (thermal) CVD. (a) Top view of vertically-aligned CNTs, inset: larger view. (b) Cross-sectional view of vertically-aligned CNTs.

1.8 Characterization of carbon nanotubes

1.8.1 Optical reflectance is the return of ray from a surface at the same wavelength as the incident ray. Optical reflectance may be specular from a very smooth surface and diffuse from a roughness of surface and or a combination of diffuse and specular reflectance as shown in Fig. 1.13. A special class of specular reflectance is of particular interest to photoelectric sensing called “Retroreflectance”. The optical reflectance does not include re-radiation by the fluorescent or thermal conversion [22].

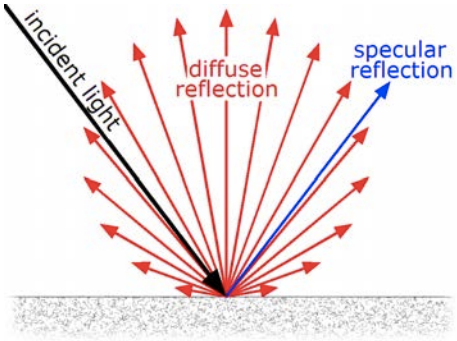

Fig. 1.13 Schematic of diffuse and specular reflectance on a surface. Reprinted from https://www.wikiwand.com/en/Diffuse_reflection

Particularly, the diffuse reflectance scatters optically on rough surface in all directions. As a light ray, being very tiny, interacts with only a microscopic scale of a target, roughly-textured surfaces present various surface orientations to incident rays. Then, the reflectance from surfaces will then also be in various directions. A diffuse reflectance expression from Lambertian reflectance called Lambertian intensity is provided as

$$I = I_0 \cos(\theta)$$

where I_0 is the incident light intensity, I is the reflected light intensity, θ it the angle between the surface normal (a line perpendicular to the surface) and the path of the radiant emission. Specular reflectance is a reflection light which quite consistently strikes and rebounds back in the same angles or to produce the visual effects of mirror reflectance. The most significant imperfections of specular reflectors are partial reflections and curved surfaces. The partial specular reflectance is most common among non-metallic surfaces. For example, the light each specularly reflect about 4 % on the front and back surface when light is transmitted by transparent glasses. The curved specular surfaces are a familiar sight on glossy paper stock, wet roads, drinking glasses, polished leather, lakes with ripples, antiglare glass, and many other objects. The curved surfaces cause the reflected image to be different. The angle of reflectance still equals the angle of incidence on the microscopic scale. As the microscopic surface is not quite flat relative to the macro surface, the macro effect is a broadened specular peak where the angle of reflection is almost the same as the angle of incidence. The specular reflectance as described by Fresnel's law:

$$R = (n - n_0)^2/(n + n_0)^2.$$

Where, n_0 is reflective index of air ($n_0 = 1.0003$), and n is a reflective index of reflected surface.

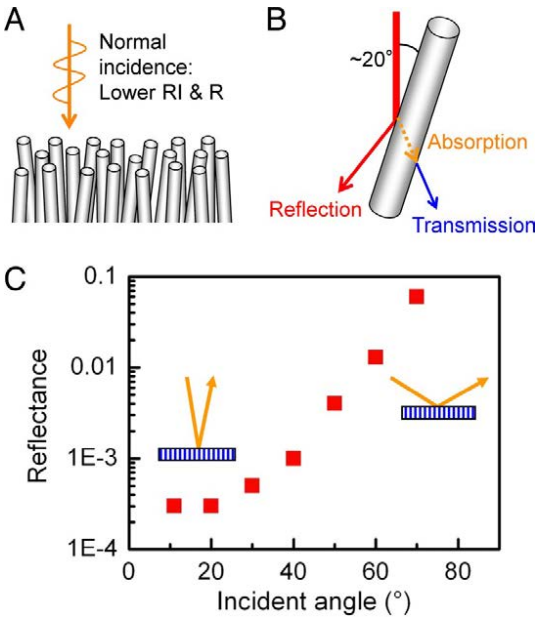

Fig. 1.14 Schematics displaying interaction between incident light and CNTs. The interaction between light and (A) CNT forest and (B) single CNT, (C) Specular reflectance vs incident angles. Reprinted from [22] with permission from PNAS.

In our research, the absorbance for the non-transparent substrates such as semiconducting silicon, 45-permalloy, stainless steel can be obtained as

$$A = 1 - R,$$

where A is the absorption and R is the total reflectance in case of transmittance (T = 0) [23]. In our experiments, the total and diffuse reflectance of CNT samples were measured whereas a detail of reflectance measurement set-up and process is described in the chapter 2.

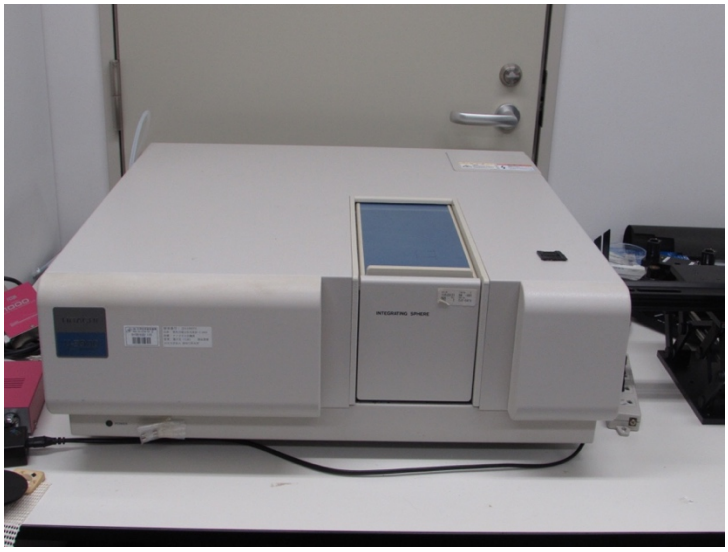

Fig. 1.15 Spectrophotometer (HITACHI U-3900, HITACHI high-technologies, Tokyo, Japan) with an integrating sphere in Nanotechnology Center, Kochi University of Technology.

1.8.2 Photoluminescence (PL) Spectroscopy: Photoluminescence spectroscopy (PL) is used to characterize PL spectra of a sample which is excited from the incidence of light. If a sample absorbs light, the electrons of sample moves from the ground to in the higher level of an excited state. After that, the electrons jump toward the lower level in the ground state with the emitting light called photoluminescence. The sample has a specific spectrum. In our experiment, we measured PL peaks of QDs-treated CNT samples with a 325-nm wavelength of He-Cd laser source as a setup equipment shown in Fig. 1.15.

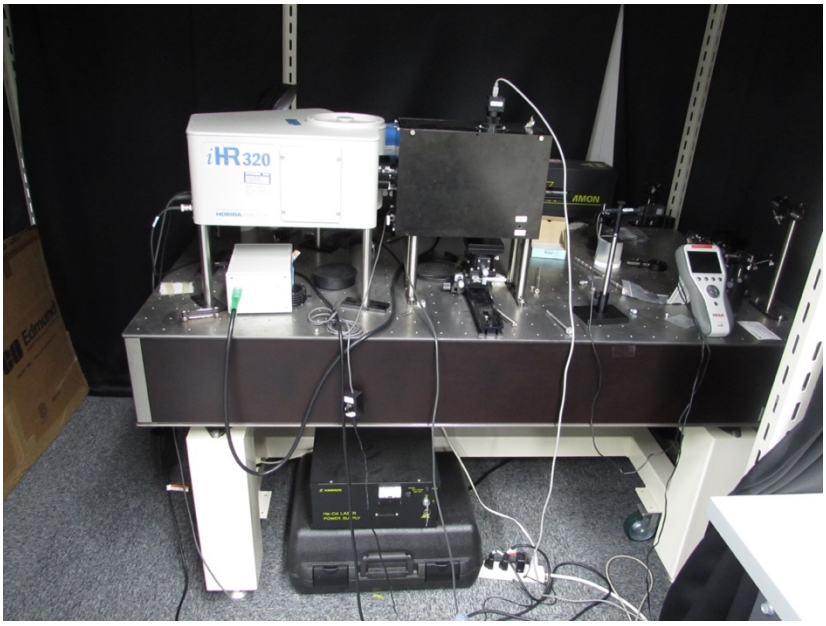

Fig. 1.16 iHR320 Micro-Pl/Raman spectroscope (Horiba) with a 325-nm wavelength of He-Cd laser source in Nanotechnology Center, Kochi University of Technology.

1.8.3 Electron Microscopy

Tomographic morphology of the CNTs have been characterized by scanning electron microscopy (SEM) and transmission electron microscopy (TEM). SEM is the most popular method to characterize the CNT forest. TEM is also the powerful method to analyze CNTs with high resolution. TEM has been widely be used since the discovery and development on CNTs. Moreover, TEM has been utilized to successfully analyze hollow properties of CNTs and crystallographic structures. Moreover, scanning tunneling microscopy (STM), and atomic force microscopy (AFM) has been used to characterize the surface structure of CNTs at atomic scale. In this research, only SEM and TEM were used to analyze the morphology of CNT forests.

1.8.3.1 Scanning Electron Microscopy (SEM): An SEM is a tool of electron microscope to characterize a sample by a high-energy beam of electrons in a raster scan mode. The principle of SEM functionality can be explained that the high-energy electrons interact with the specimen atoms to produce signals that contain profile about the specimen's surface topography, composition, and electrical conductivity etc. The types of signals produced by an SEM include secondary electrons, back-scattered electrons, characteristic X-rays, cathodoluminescence,

specimen current, etc. Secondary electron imaging (SEI) is the the most common detection mode in SEM and widely employed to observe the morphology of CNTs. Figure 1.35 schematically illustrates the basic principle of the SEI that a very fine beam of high-energy electrons (20–40 keV) is focused on the specimen surface and scanned across the specimen in a raster. When electrons with the high-energy of the beam bombard onto the specimen, some incident electrons will strike the electrons in the k-orbits of the specimen atoms (inelastic scattering) to release free electrons with very low energy (< 50 eV), secondary electrons, while some are elastically scattered by the specimen atoms. More secondary electrons will be released until the high-energy electrons devoid of energy when the high-energy electrons travel deeper into the specimen undergoing multiple inelastic collisions. These released secondary electrons can only travel a few or tens nanometers from the specimen surface. Therefore, SEI can give the tomographic information (several nanometers) of samples.

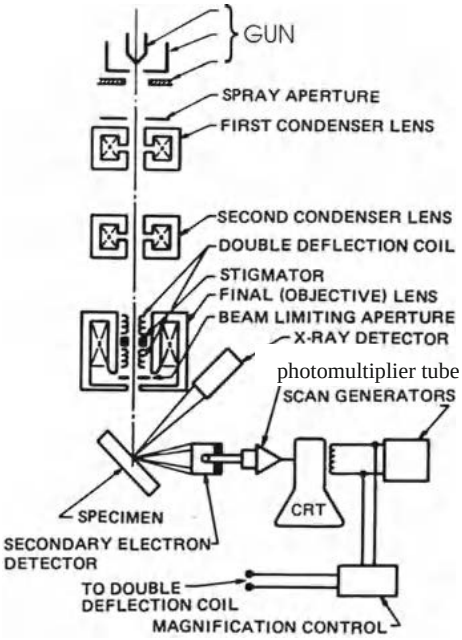

(a) **(b)**

Fig. 1.17 A SEM equipped with an energy dispersive X-ray spectrometer in Nanotechnology Center, Kochi University of Technology, JEOL-JSM7400F SEM.

SEI, a no-destroyed method, has a large depth of field on the order of millimeters due to the very narrow electron beam. The observation method is direct and simple. Due to these advantages, SEI has been widely used to analyze the morphology of aligned CNTs, including CNT heights, diameters, and CNT site spacing. The SEM usually operates at 20 kV for better resolution depending on the electrical conductivity of CNT and substrates. To avoid the electric discharging during observation, 5 kV or lower is also used. The CNT heights, diameter, CNT site spacing have been qualitatively carried out on the aligned CNTs. However, the qualitative measurement of CNT alignment degree from SEI images are time-consuming. For our image analysis, we ultilized FE-SEM to characterize CNTs and QDs-CNTs morphologies as well as physical parameters such as heights of CNT, honeycomb cell areas, diameters, density etc were calculated with ImageJ software use.

1.8.3.2 Transmission Electron Microscopy (TEM): High resolution TEM (HRTEM), is also a powerful tool to directly observe the alignment of CNTs with a fine resolution to nanometers. However, TEM is a destructive technique. Since we scratch the CNTs off from the substrates for TEM specimens, the alignment structure of CNTs, especially the relative position between aligned CNTs, are usually changed. In order to protect a destruction of the original spatial structure of aligned CNTs, the aligned CNTs can be immersed in solutions e.g. ethanol or epoxy. After cured, the aligned CNTs/epoxy or ethanol is mechanically polished and ion milled to be TEM specimen, as in a traditional cross-sectional TEM specimen preparation procedure.

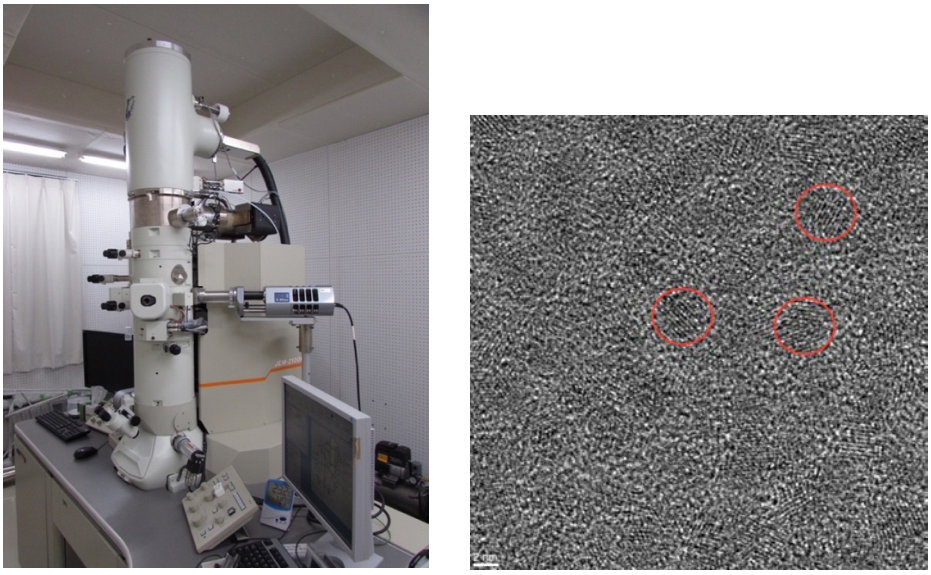

(a) **(b)**

Fig. 1.18 (a) A TEM equipment in Center for Nanotechnology, Kochi University of Technology, The JEOL-2100F TEM system (b) TEM image of CdSe/ZnS core/shell QDs.

The TEM technique can give direct results with much higher resolution and precision as compared with other techniques. However, the preparation of TEM specimen and the observation are time-consuming. In our TEM observation, the QDs-treated CNTs for solar cells were characterized to observe the QD diameters and existing QDs as Fig. 1.18(b).

1.9 QDs-CNT Solar cell fabrication and I-V characteristics analysis

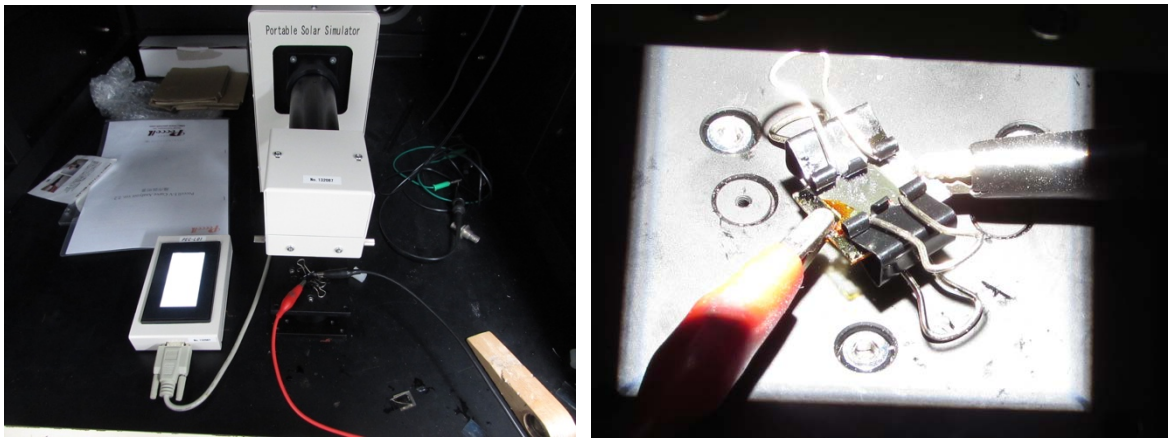

(a) **(b)**

Fig. 1.19 (a) Photocurrent density vs. voltage curve and the equation for fill factor, (b) Portable solar simulator tool, (c) Measurement of QD-CNTs solar cell sample.

In our experiments, the QDs-CNT solar cells process of fabrication is as follows:

1. Solar cells were assembled CdSe/ZnS core/shell QDs-CNT nanostructures as the photoanode in various CNT substrates for efficiency comparison.

2. A counter electrode was prepared using a conductive indium tin oxide (ITO) glass.

3. The ITO counter electrode and the CdSe/ZnS core shell QDs-CNTs were sandwiched and sealed with the two-sided scotch tapes.

4. An iodide electrolyte solution (I_1^-/I_3^-) was injected into the cell active area (space) between the two electrodes.

5. A solar simulator (model 2400, Keithley) an AM1.5 filter was used to illuminate the working solar cell at light intensity of 1 sun illumination (100 mW/cm^2) as shown in Fig. 1.19(a). A sourcemeter was carried out for electrical characterization during the measurements, as can be seen in Fig. 1.37(b) to obtain I-V curves, fill factors (FF), open voltage (Voc), short current (Isc), and efficiency (η) as the mentioned expression: $\eta = P_{max}/P_{in} = J_{sc}\, V_{oc}\, FF/ P_{in}$.

REFERENCES

[1] S. Iijima, “Helical microtubules of graphitic carbon,” *Nature*, vol. 354, no. 6348, pp. 56–58, Nov. 1991.

[2] M. S. Dresselhaus, G. Dresselhaus, and R. Saito, “Physics of carbon nanotubes,” *Carbon N. Y.*, vol. 33, no. 7, pp. 883–891, 1995.

[3] T. Sugai *et al.*, “Syntheses of single- and double-wall carbon nanotubes by the HTPAD and HFCVD methods,” *New J. Phys.*, vol. 6, no. 1, pp. 21–21, Feb. 2004.

[4] R. T. K. Baker, “Catalytic growth of carbon filaments,” *Carbon N. Y.*, vol. 27, no. 3, pp. 315–323, 1989.

[5] K. E. Jasim, “Dye Sensitized Solar Cells - Working Principles , Challenges and Opportunities,” *B. Chapter*, 2007.

[6] A. . Nozik, “Quantum dot solar cells,” *Phys. E Low-dimensional Syst. Nanostructures*, vol. 14, no. 1–2, pp. 115–120, 2002.

[7] A. Franceschetti, J. M. An, and A. Zunger, “Impact ionization can explain carrier multiplication in PbSe quantum dots,” *Nano Lett.*, vol. 6, no. 10, pp. 2191–2195, 2006.

[8] A. J. Nozik, M. C. Beard, J. M. Luther, M. Law, R. J. Ellingson, and J. C. Johnson, “Semiconductor quantum dots and quantum dot arrays and applications of multiple exciton generation to third-generation photovoltaic solar cells,” *Chem. Rev.*, vol. 110, no. 11, pp. 6873–6890, 2010.

[9] E.-H. Kong, Y.-J. Chang, and H. M. Jang, “Hierarchically Nanostructured Photoelectrodes for Quantum-Dot-Sensitized Solar Cells,” in *QUANTUM DOT SOLAR CELLS*, vol. 15, 2014, pp. 39–66.

[10] P. V. Kamat, “Quantum Dot Solar Cells. Semiconductor Nanocrystals as Light Harvesters †,” *J. Phys. Chem. C*, vol. 112, no. 48, pp. 18737–18753, Dec. 2008.

[11] P. Brown and P. V. Kamat, “Quantum dot solar cells. Electrophoretic deposition of CdSe-C60 composite films and capture of photogenerated electrons with nC60 cluster shell,” *J. Am. Chem. Soc.*, vol. 130, no. 28, pp. 8890–8891, 2008.

[12] L. Sheeney-Haj-Ichia, B. Basnar, and I. Willner, “Efficient generation of photocurrents by using CdS/carbon nanotube assemblies on electrodes,” *Angew. Chemie - Int. Ed.*, vol. 44, no. 1, pp. 78–83, 2004.

[13] Q. Huang and L. Gao, “Synthesis and characterization of CdS/multiwalled carbon nanotube heterojunctions,” *Nanotechnology*, vol. 15, no. 12, pp. 1855–1860, 2004.

[14] A. Luque and S. Hegedus, *Handbook of Photovoltaic Science and Engineering*. 2011.

[15] B. O’Regan and M. Grätzel, “A low-cost, high-efficiency solar cell based on dye-sensitized colloidal TiO2 films,” *Nature*, vol. 353, pp. 737–740, 1991.

[16] Z. A. Peng and X. Peng, “Formation of high-quality CdTe, CdSe, and CdS nanocrystals using CdO as precursor [6],” *Journal of the American Chemical Society*, vol. 123, no. 1. pp. 183–184, 2001.

[17] H. J. Lee *et al.*, “CdSe quantum dot-sensitized solar cells exceeding efficiency 1% at full-sun intensity,” *J. Phys. Chem. C*, vol. 112, no. 30, pp. 11600–11608, 2008.

[18] J. H. Bang and P. V. Kamat, “Quantum dot sensitized solar cells. A tale of two semiconductor nanocrystals: CdSe and CdTe,” *ACS Nano*, vol. 3, no. 6, pp. 1467–1476, 2009.

[19] L. Chen, J. Wei, C. Zhang, Z. Du, H. Li, and W. Zou, “Synthesis of a carbon quantum dots functionalized carbon nanotubes nanocomposite and its application as a solar cell

active material," *RSC Adv.*, vol. 4, no. 93, pp. 51084–51088, 2014.
[20] J. E. Mahan, *Physical Vapor Deposition of Thin Films*. 2000.
[21] D. L. Smith and D. W. Hoffman, *Thin-Film Deposition: Principles and Practice*, vol. 49, no. 4. 1996.
[22] K. Mizuno *et al.*, "A black body absorber from vertically aligned single-walled carbon nanotubes," *Proc. Natl. Acad. Sci.*, vol. 106, no. 15, pp. 6044–6047, 2009.
[23] M. Peters, C. Ulbrich, J. C. Goldschmidt, J. Fernandez, G. Siefer, and B. Bläsi, "Directionally selective light trapping in a germanium solar cell," *Opt. Express*, vol. 19, no. S2, pp. A136–A145, 2011.

CHAPTER 2

Carbon Nanotube (CNT) Honeycomb Cell Area-Dependent Optical Reflectance

Abstract: The relationship between the physical structure of carbon nanotube (CNT) honeycomb structures and their total, diffuse, and specular reflectance is investigated for the first time. It is found that CNT honeycomb structures with average cell areas of smaller than 30 μm^2 show a higher total reflectance. Particularly, a thinner, highly packed CNT (buckypaper) film, along with a larger wall height and higher ratio of wall height to cell area, markedly increase the total reflectance for cell areas smaller than 30 μm^2, which means that a higher total area of buckypapers in CNT walls and bottom areas increases the total reflectance, including the diffuse reflectance. It is also found that the total reflection of non-absorbed light in CNT honeycomb structures consists primarily of diffuse reflectance.

2.1 Research background and Literature review

Unique morphologies and structures of carbon nanotubes (CNTs) have received much attention in optical and electronic applications because CNTs provide extraordinarily photonic properties, highly electrical current endurability, and mechanical stiffness [1]–[4]. Morphologies of CNT forests can also be modified to enhance charge generation, separation, and transport in optical-electronic applications [5]. In order to modify CNT forest morphologies, a liquid or vapor treatment is one of simple methods to provide an economical cost and a high yield. The liquid treatment of CNTs shows a self-assembly to build one-dimensional material into 3D micro or macro engineering with various morphologies [5], [6]. Previous papers reported that the liquid and vapor treatment onto multi-walled CNTs (MWCNTs) shows self assembly as hierarchical networks to form honeycomb structures due to capillary forces arisen during solution evaporation [7]–[10]. A larger surface area of honeycomb structures is expected to assemble sensitized nanoparticles of quantum dots (QDs) efficiently, which are served as an electrode scaffold to capture and transport photo-generated electrons in solar cells [11]. Additionally, in the structure of silicon solar cells with CNT honeycomb top electrodes, a spacing area in honeycomb structures allows higher transmission of the light to photo-active parts of solar cells when light irradiation is perpendicular to a substrate [12]. Moreover, wall-shaped condensed CNT films serve “an electron–carrying highway” enhancing high conductivity to an electrode of solar cells [5].

Ajayan et al reported extraordinary low total reflectance of 0.045 % for the mat of vertically aligned multi-walled carbon nanotubes (VA-MWCNTs) forests in a visible region at specific wavelengths of 457 – 633 nm [13]. The total reflectance of randomly–oriented CNT–

compressed sheets is 30 – 40 % [14] while high nanotube forests (300 – 500 μm in height) is 1 – 2 % across an entire specified range of UV-to-near IR and Near-to-Mid IR (200 – 2000 nm) [15]. Theoretically, for the relationship between the reflectance and CNT forests, it can be explained during light incidence to a forest top surface of CNTs, in case an angle of light incidence and a CNT axis is smaller, electrons on CNT body can not couple with electric fields [13], [15]. This will provide a weak optical interaction between CNT forests and normally incident light resulting the lower total reflectance[16].

For photovoltaic applications, optical properties are one of the most important parameters to render light enhancement. Recently, it has been reported that reuse of optical reflectance of existing light to significantly increase the efficiency in dye sensitized solar cells (DSSC) [17]. To date, previous works have not been reported to benefit relationship between the optical reflectance and CNT honeycomb structures. Utilizing the highly-reflected light from CNTs is expected to be absorbed by sensitizers generating more electron-hole pairs in solar cells.

In this chapter, the relationship between the total, diffuse, and specular reflectance and CNT honeycomb structures were unveiled for the first time. CNT honeycomb structures were fabricated and cell areas can be controlled by a simple method of ethanol treatment. This chapter aims to investigate the total, diffuse, and specular reflectance influenced by CNT honeycomb structures. In particular, honeycomb structures including a cell area, a wall height-to-whole area ratio (surface area), bottom area-to-whole area ratio (total bottom areas with respect to whole cell area), a wall height, and a buckypaper film thickness were investigated to show an influence on the reflectance.

2.2 Material and methods

CNT forests were prepared using a method from our previous work, with a CNT density of ~8.0 × 109/cm^2 and wall heights of ~10 μm by a 20-s synthesis on AlOx/Fe bi-layered catalyst films (30 nm/1 nm in thickness) on a silicon substrate using a thermal chemical vapor deposition (thermal-CVD) system at 730 ◦C with a C_2H_2 gas source at 54 Pa [18]. In order to fabricate honeycomb structures and control the cell areas, CNT forest samples with of 1.5 cm^2 area were treated with varying volumes of 98.5% ethanol from 5, 10, 15, 20, 25, and 30 μL in an ambient environment until the ethanol was completely evaporated. The longer evaporation times of larger

volumes of ethanol provided larger average cell areas of CNT honeycomb structures as shown in Fig. 2.1. The morphologies of as-synthesized CNT forests and CNT honeycomb structures were characterized by field-emission scanning electron microscope (FE-SEM) (JEOL JSM-5310, JEOL Ltd., Tokyo, Japan). Evaluation of the cell areas, wall heights, bottom areas, and buckypaper film thicknesses at the bottom areas was quantitatively performed by the image processing software ImageJ (National Institutes of Health (NIH), Bethesda, MA, USA) [19]. The total and diffuse reflectance from UV through visible regions (190 - 900 nm) was measured using a spectrophotometer (HITACHI U-3900, HITACHI high-technologies, Tokyo, Japan) with an integrating sphere.

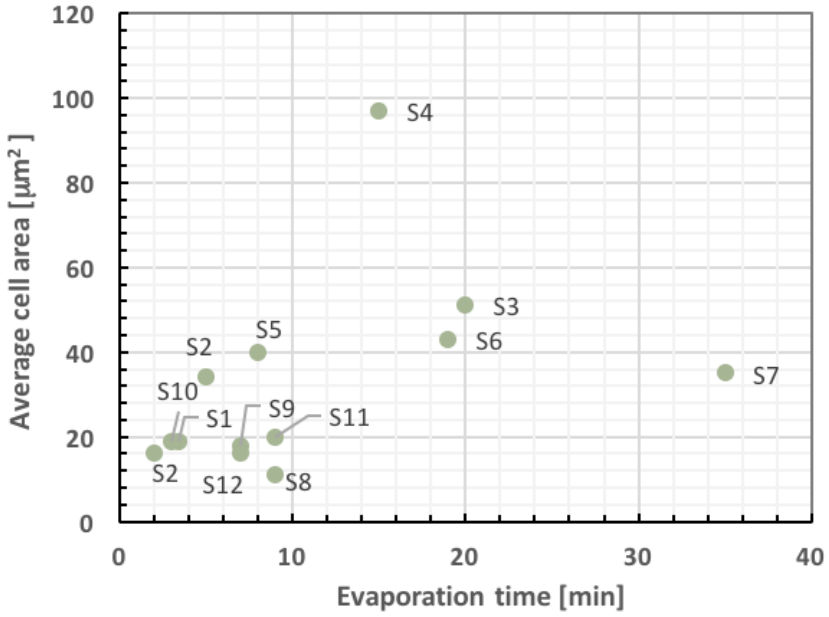

Fig. 2.1 A plot of average cell areas as a function of ethanol evaporation time at the room temperature during fabrication of CNT honeycomb structures. Reprinted from [20].

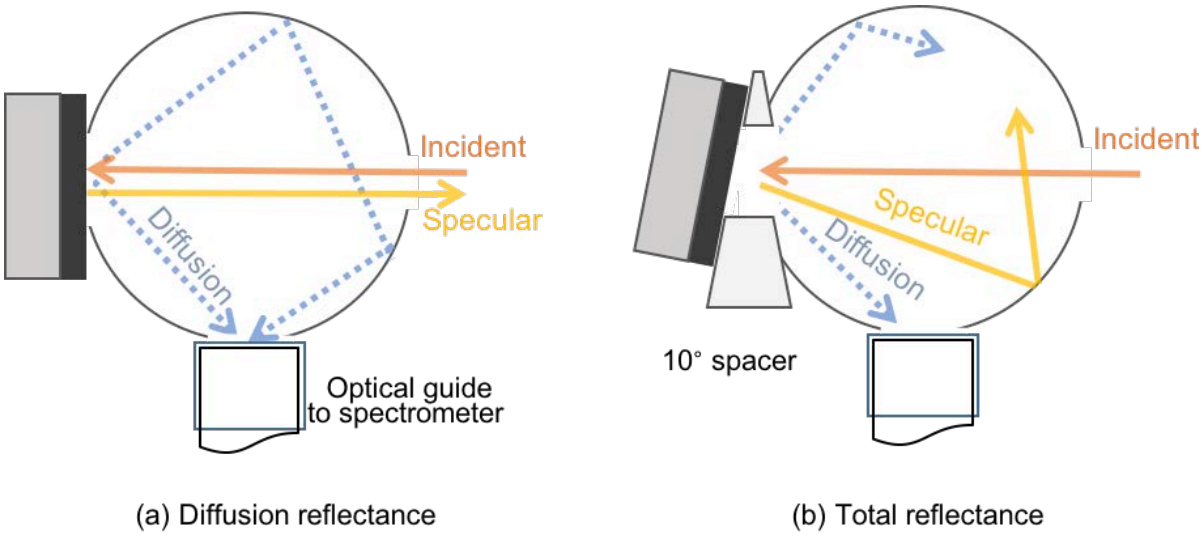

Fig. 2.2 Configuration of measurement for (a) diffuse reflectance by 0° tilt (b) total (diffuse + specular) reflectance by a 10° spacer tilted away from the light incidence with an integrating sphere. Incident light (orange), specular reflectance (yellow), and diffuse reflectance (dashed blue).

Figure 2.2 (a) displays a measurement setup with the integrating sphere for (a) the diffuse and (b) total reflectance including diffuse (dashed blue arrows) and specular (yellow arrows) reflectance where a regular sample is 0° and 10° tilted away from a direction of light incidence (orange arrow) for measurement of the diffuse and total reflectance, respectively. The diffuse measurement in Fig. 2.2(a) illustrates that reflected light as the specular reflectance from a non-tilted sample is directly reflected back through an open window, whereas the total reflectance in Fig. 2.2(b) includes both of specular and diffuse reflectance [21].

2.3 Results and Discussions

2.3.1 Morphologies of CNT honeycomb structures

Figure 2.1(a) displays a top-view of an FE-SEM micrograph of as-synthesized CNTs with mean diameter of 10 – 15 nm. A lower image of Fig. 2.1(a) shows a cross section image displaying vertically-aligned CNTs with heights of ~10 μm. CNT forests show a uniformly flat surface (Fig. 2.1(a)), in which CNTs exhibit random entangles each other, tip bending and a loosely connected random surface as seen in the larger magnification in an inset of Fig. 2.1(a). FE-SEM images and cell area histograms for honeycomb CNT Samples 1, 2, 3, and 4 with averaged cell areas of 19, 34, 51 and 97 μm2 are shown in Fig. 2.1(b–f), respectively. After ethanol treatment, as can be seen in a top view of CNT forests in Fig. 2.1(b–e), self–assembling honeycomb structures were formed by attractive force of an aggregation due to capillary forces [7]–[10]. A honeycomb cell composes main two parts including vertically standing CNT walls and a collapsed CNT mat on a bottom area. These CNT walls and the collapsed CNT mat on the bottom area are composed by CNTs called buckypapers.

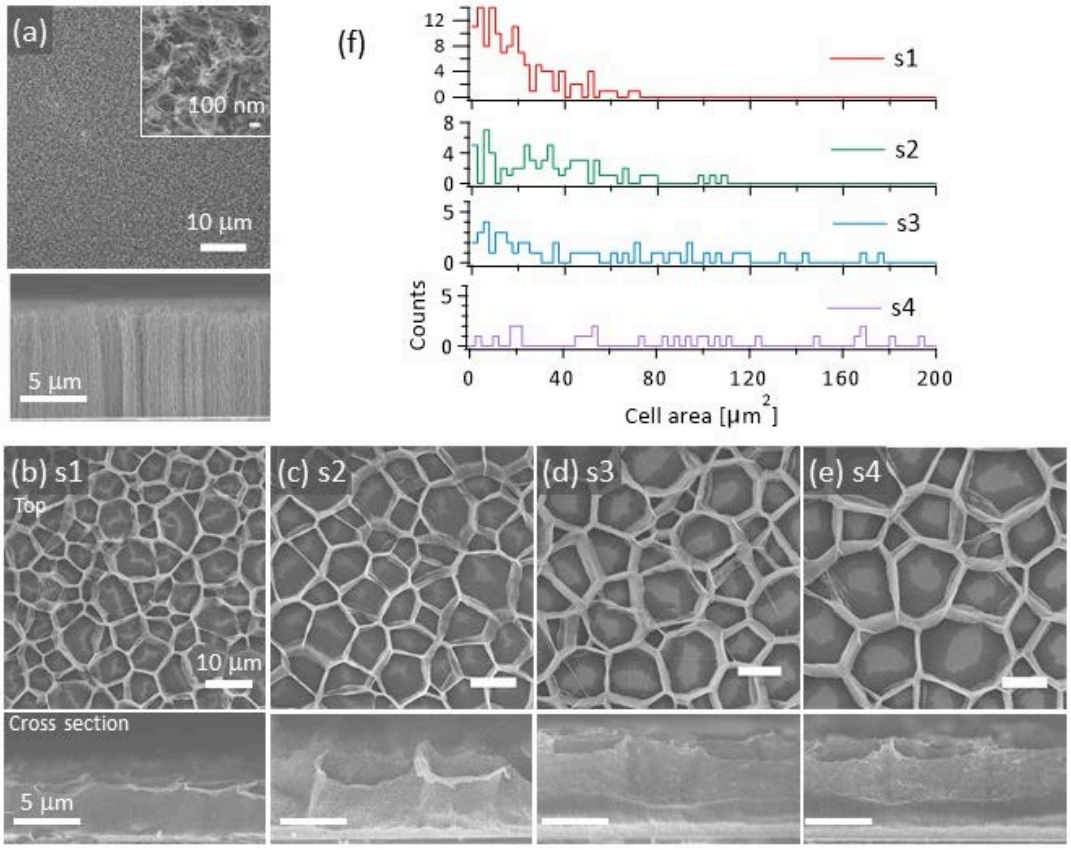

Fig. 2.3 (a) Top-view FE-SEM micrographs of as-synthesized CNTs, a highly-magnified image of vertically-aligned CNT forests of as-synthesized CNT forests displayed displayed in an upper-right inset and a cross-section in a lower image. Top-view (above) and cross-section (below) of FE-SEM micrographs of CNT honeycomb structures for (b) S1 (16 μm^2), (c) S2 (34 μm^2), (d) S3 (51 μm^2), (e) S4 (97 μm^2). (f) Histogram of CNT honeycomb cell area. Reprinted from [20].

As shown in a lower image of Fig. 2.3(b), honeycomb cells of Sample 1 (S1) are polygons including few triangle patterns and mainly quadrangular, pentagon and hexagon structures with wall heights varying from 2.9 to 4.4 μm (3.7 μm in average). Average cell areas of CNT honeycomb structures for S1 are 19 μm^2 and a cell area distribution is shown in a red histogram of Fig.1(f). As depicted in each honeycomb cell in all S1– S4 samples, the bottom area at the center shows a catalyst composed–silicon substrate as especially clearly seen in Fig.1(d–e). Thicknesses of CNT buckypaper films near the silicon area at the center toward to the CNT wall are 0.47 μm in average in S1 as shown in a lower image of Fig. 2.3(b). Sample 2 (S2) shows larger average cell areas of 34 μm^2 with higher inconsistent wall heights of 3.7 μm in average

and CNT buckypapers film thicknesses of 0.58 μm in average as displayed in a lower image of Fig.1(c). Sample 3 (S3) shows much larger cell areas of 51 μm^2 with higher wall heights of 7.2 μm in average, and CNT buckypapers film thicknesses of 0.89 μm in average as displayed in Fig. 2.1(d). Sample 4 (S4) shows largest honeycomb cell areas of 97 μm2 with the longest wall heights of 7.9 μm in average in cross-sectional image of Fig. 2.1(e) and the CNT buckypaper film thicknesses varying from 1.0 μm in average.

Table 2.1 Comparison of parameters of as-synthesized CNTs and samples S1–S13 of CNT honeycomb structures. R_T: total optical reflectance, R_D: diffuse optical reflectance, UV: ultraviolet, Vis: visible [20].

Samples	% R (UV)		% R (Vis)		cell size (μm^2)	wall height-to-cell size ratio	bottom area-to-cell size ratio	wall height (μm)	buckypaper film thickness (μm)
	R_T	R_D	R_T	R_D					
As-synthesized CNTs	0.5	0.7	1.0	0.4	–	–	–	~10	–
Sample 1	11	11	7.1	6.5	19	0.20	0.52	3.7	0.47
Sample 2	8.2	8.2	6.3	6.5	34	0.11	0.60	3.7	0.58
Sample 3	9.4	8.5	7.9	7.3	51	0.14	0.57	7.2	0.89
Sample 4	9.5	8.3	8.4	7.3	97	0.08	0.61	7.9	1.0
Sample 5	7.7	7.0	6.1	5.9	40	0.07	0.57	2.7	1.0
Sample 6	7.5	7.5	6.3	6.2	43	0.08	0.56	3.5	0.38
Sample 7	6.2	5.6	5.2	5.0	35	0.12	0.53	4.1	0.61
Sample 8	7.9	6.8	6.3	6.1	11	–	0.49	–	–
Sample 9	11	9.1	8.0	7.1	18	–	0.52	–	–
Sample 10	11	11	7.6	7.8	19	–	0.53	–	–
Sample 11	7.8	7.7	6.4	6.1	20	0.14	0.53	2.9	0.55
Sample 12	12	8	8	6.3	16	0.28	0.56	4.4	0.5
Sample 13	10	7	6.9	5.8	16	0.34	0.47	5.5	0.2

2.3.2 Total, diffuse, and specular reflectance

In the mechanism of interaction between the light and CNT forests, the incident light irradiates to vertically-aligned CNT forests, in which the light can be absorbed, transmitted and reflected on CNT individuals [5]. The total reflectance of as-synthesized CNT forests, all of 4

samples of CNT honeycomb structures, and the silicon substrate is plotted in Fig. 2(a–c). It exhibits that as-synthesized CNT forests as vertically-aligned CNT forests with height of 10 μm demonstrates the low reflectance of 0.5 % in average (Also see Table 1) at the UV region (black line) in Fig. 2(b). It is observed that this result shows a similarity to a previous finding which also shows the low reflectance across the UV region (190 – 380 nm) due to a multiplication of light reflectivity regardless of very high nanotube forests of 300 – 500 μm [15]. A dip at a wavelength of 236 nm (5.3 eV) on a reflectance curve correspond to an absorption peak attributed to a π-plasmon peak of CNTs [16]. In the visible region (380 – 900 nm), the result shows that the reflectance of as-synthesized CNT forests is 1.0 % in average, which is higher than in the UV region. As Murakami et al [16] reported that vertically-aligned CNTs have the lower light absorption of lower photon energy in the visible region, this supports our result, as-synthesized CNTs, showing that the higher total reflectance in the visible region compared with UV region.

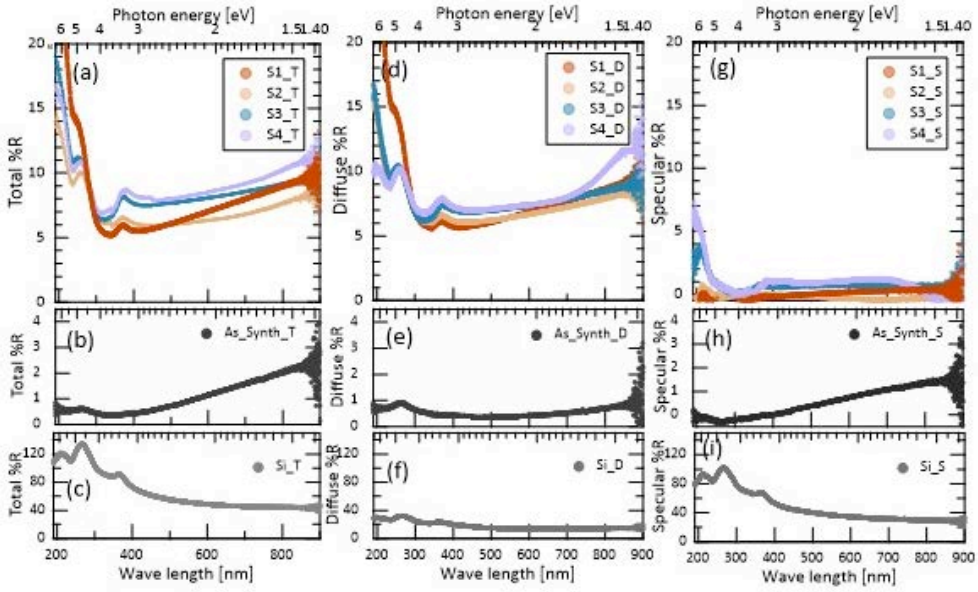

Fig. 2.4 Total reflectance (Total %R), diffuse reflectance (Diffuse %R), and specular reflectance (Specular %R) of CNT honeycomb structures as the function of UV-visible wavelengths (nm) and photon energy (eV) for S1 (red), S2 (orange), S3 (blue) and S4 (violet) in Fig. 2(a), (d), (g), as-synthesized CNT forests (black) in Fig. 2(b), (e), (h), and a silicon substrate (grey) in Fig. 2(c), (f), (i), respectively. Reprinted from [20].

After ethanol treatment, in the UV region the average total reflectance of CNT honeycomb structures of S1 (red), S2 (orange), S3 (blue), and S4 (violet) shows 11 %, 8.2 %,

9.4 %, and 9.5 %, respectively. Besides, it is clear that such two additional peaks observed in CNT honeycomb structures at 270 and 380 nm are attributed to a silicon substrate [21], [22]. This result shows that silicon peak height is reduced by the light absorption of CNT-formed honeycomb structures. In the visible region of 380 – 900 nm, the total reflectance of CNT honeycomb structures in S1, S2, S3 and S4 provides lower average values of 7.1 %, 6.3 %, 7.9 %, and 8.4 %, respectively. The total, diffuse, and specular reflectance in the UV region provide values higher than in the visible region as shown in Fig. 2.4 (a, d, g). This behavior is likely a result of a silicon substrate indicating the low total reflectance (high photon absorption) in this visible region of 380 - 900 nm which is correspondent to the wavelength absorption range of silicon (1.12 eV) [13]. It can be interestingly noticed that smaller cell area of S1 gives the higher total reflectance as compared with larger cell areas of S2, S3 and S4 in the UV region, but shows the lower total reflectance in the visible region as shown in Fig. 2.4(a). To explain this phenomenon of higher total reflectance in S1 at the higher energy light region, this result is needed to be interpreted at the viewpoint of physical structure of honeycomb network in details in the section 2.3.3.

The diffuse reflectance of as-synthesized CNT forests, 4 samples of CNT honeycomb structures, and the silicon substrate were observed as shown in plots of Fig. 2(d–f). It can be observed that the diffuse reflectance of as-synthesized CNTs shows a value at 0.7 % as compared with the total reflectance of 0.5 % in the UV region. In the visible region, the diffuse reflectance of as-synthesized CNTs shows a lower value at 0.4 % as compared with the total reflectance of 1.0 %. In CNT honeycomb structures, the diffuse reflectance of S1 with the smallest cell area surprisingly demonstrates the highest values of 11 % as compared with S2, S3, and S4 in the UV region, and provides the low reflectance of 6.5 % in the visible region. Interestingly, it can be noticed that all the diffuse reflectance of S1 -S4 does not show a big difference as compared to the total reflectance especially in S1 and S2 exhibiting the values of 11 % and 8.2 % in the UV region, respectively. This interesting result is also needed to be interpreted at the viewpoint of physical structure of honeycomb network in details in the section 3.3.

The difference between the total and diffuse reflectance ($R_T - R_D$) which represents the specular reflectance (R_S) as calculated from $R_T = R_D + R_S$ (R_T = total reflectance, R_D = diffuse

reflectance, and R_S = specular reflectance) of S1 – S4, as-synthesized CNT forests, and the silicon substrate is plotted in Fig. 2.4(g – i). In the UV region, the specular reflectance of as-synthesized CNTs shows a value of 0.2 % lower than the total and diffuse reflectance of 0.5 % and 0.7 %, respectively. In the visible region, the specular reflectance of as-synthesized CNTs shows a value at 0.6 % closer to the total and diffuse reflectance of 1.0 % and 0.4%, respectively. In CNT honeycomb structures, the specular reflectance of S1 shows a non-value of 0 % while the larger cell area of S2, S3, and S4 gives a small change of the specular reflectance of 0.0 %, 0.9 %, and 1.2 %, respectively in the UV region. In the visible region, the specular reflectance of all samples S1-S4 exhibits no much more difference up to 1.1 %.

In CNT honeycomb structures, due to the high diffuse reflectance, it can be noticed that the specular reflectance show very small values as compared to the total and diffuse reflectance. More analysis according to the relationship between cell areas and the specular reflectance is given in a coming section 2.3.3.

2.3.3 CNT honeycomb cell areas vs total, diffuse and specular reflectance

A plot of Fig. 2.5 (a) shows the average total reflectance as a function of CNT honeycomb cell areas for S1 – S13, and summarized in Table 1, and their histograms and SEM images displayed in Fig. 2.6. As can be seen, a group of samples in S2, S3, S4, S5, S6, and S7 with cell areas larger than 30 μm^2 shows a tendency to increase the total reflectance in both UV and visible regions. In a contrary, it can be noticed that the total reflectance of cell areas smaller than 30 μm^2 in S1, S9, S10, S12, and S13 shows higher values of 11 %, 11 %, 11 %, 12 %, and 10 % in the UV region and 8.0 %, 7.6 %, 6.4 %, 8.0 %, and 6.9 % in the visible region, respectively. In addition, a plot of Fig. 2.5 (b) shows the average diffuse reflectance as a function of honeycomb average cell areas. The data also show that CNT honeycomb structures with cell areas larger than 30 μm^2 has a tendency to increase the diffuse reflectance. Nevertheless, as shown, the diffuse reflectance of cell areas smaller than 30 μm^2 shows also higher values especially in S1, S9, and S10. Figure 2.5(c) shows the average specular reflectance as a function of cell areas. Cell areas larger than 30 μm^2 also provide the tendency to increase the specular reflectance by increasing cell areas. The specular reflectance of cell areas smaller than 30 μm2 dramatically shows the increased values especially in S12 at 4.0 % and 1.7 % in UV and visible

regions, respectively. As can be observed in Fig. 2.5(c), it is clearly seen that the data gives very small values of specular reflectance which represents non-different values between the total and diffuse reflectance in the UV region, and a very small difference of 0.1 % in the visible region in S6. Our finding shows that the difference between the total and diffuse reflectance is very small. It can be described that each honeycomb structure cell including walls and buckypaper films is served as a roughness to reflect the light, thus the incident light can be mostly scattered as the diffuse reflectance. This can lead to obviously conclude that the light, which mostly reflects on the honeycomb structures, is the diffuse reflectance.

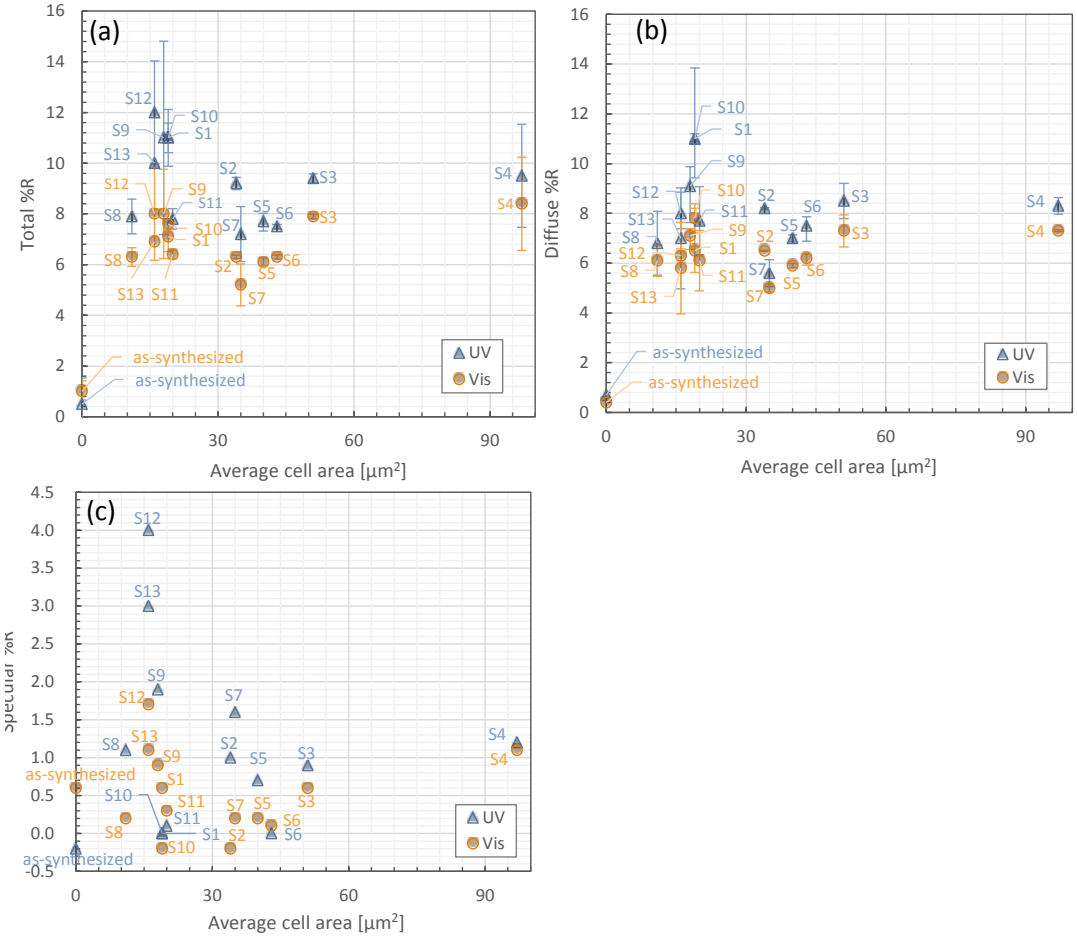

Fig. 2.5 Plots: (a) Total reflectance (Total %R); (b) Diffuse reflectance (Diffuse %R); and (c) Specular reflectance (Specular %R) as a function of average honeycomb cell area. Reprinted from [20].

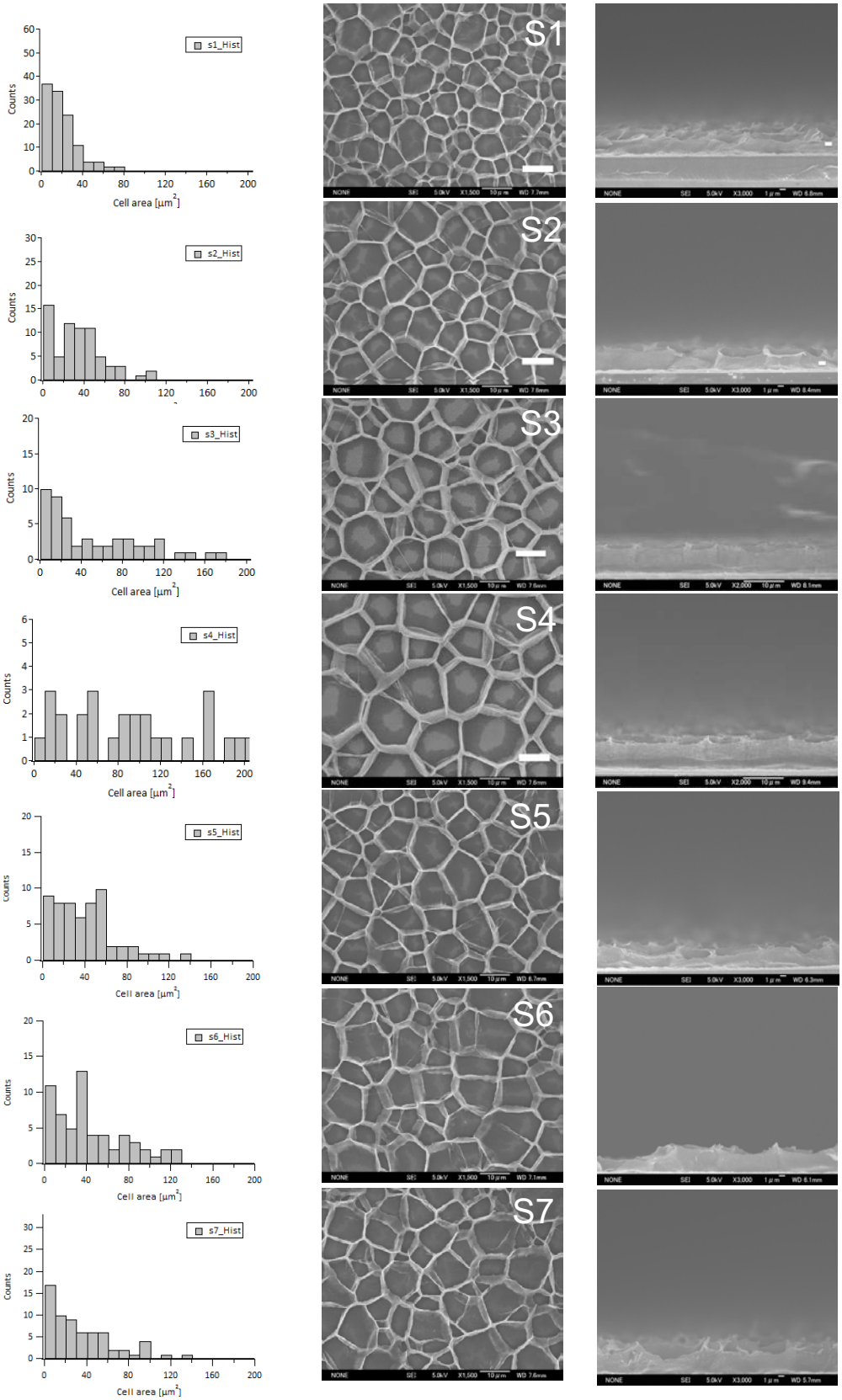
s1_Hist
Counts
Cell area [μm²]
S1
s2_Hist
S2
s3_Hist
S3
s4_Hist
S4
s5_Hist
S5
s6_Hist
S6
s7_Hist
S7

(Continued)

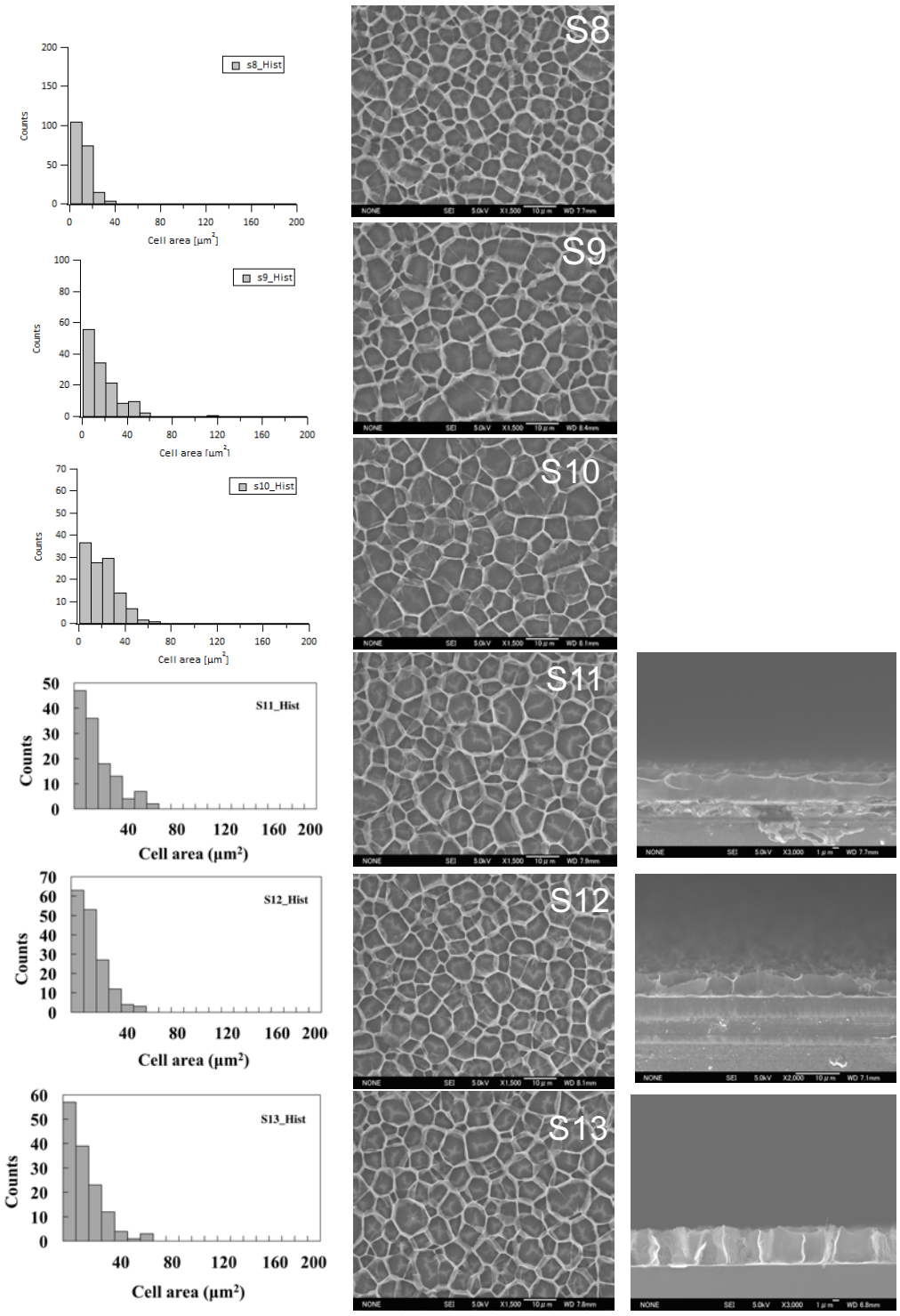

Fig. 2.6 Histograms of cell areas, top-view and cross-sectional SEM images for S1-S13

To investigate why cell areas smaller than 30 μm^2 show the higher reflectance, a physical structure of wall heights-to-whole area ratio, a bottom area-to-whole area ratio, a wall height and a buckypaper film thickness of honeycomb structures to influence the total and diffuse reflectance is discussed in a following section 2.3.4.

2.3.4 Cell areas smaller than 30 μm^2 with the higher reflectance

In order to investigate the higher total, diffuse, and specular reflectance in cell areas smaller than 30 μm^2, we consider the physical structure of the honeycomb networks. Figure 4a shows the wall height to cell area ratio (surface area) as a function of cell area. The ratio of wall height to cell area is higher in cell areas smaller than 30 μm^2 (indicated by green circles with blue outlines), with S13 (average cell area 16 μm^2) having the highest ratio of 0.34 μm^{-1}. In particular, as displayed in Figure 5a, the height to whole area ratio in S1, S12, and S13 corresponds to a high total reflectance in both the UV (green triangles) and visible (orange circles) regions. Moreover, Figure 2.5d shows that S12 and S13 have high specular reflectance in both the UV and visible regions. Thus, the study shows that a higher wall height and a very small cell area (larger surface area) give a higher reflectivity, resulting in higher total, diffuse, and specular reflectances. However, other CNT honeycomb physical structures may also lead to a high total and specular reflectance, and they are investigated below.

This relationship between the total reflectance and the wall height to cell area ratio may help explain the high total reflectance of S1 compared to S2–S4 in the UV region. Meanwhile, in the visible region, S1 has the lower total reflectance than S2–S4 because of a lower ratio of wall height to cell area. As shown in Figure 2.8g, the diffuse reflectance is not dependent on wall height to cell area.

Figure 2.7b) shows a plot of the bottom area to whole area ratio as a function of cell area. The average cell area of 16 μm^2 in S13 with the high total reflectance provides a lower ratio of 0.47 μm. A lower specular reflectance is expected for a lower ratio of bottom area to whole area for cell sizes smaller than 30 μm^2 because the higher CNT walls with smaller bottom areas will interfere with the specular reflectance. However, our results show the opposite, with a higher specular and total reflectance for the group with smaller cell areas with a lower ratio of bottom area to whole area. To interpret this unexpected result, the wall height as a function of cell area is

analyzed as follows. Based on the plot of the average wall height as a function of cell area in Figure 2.4c, S13, with a cell area smaller than 16 μm^2 and a high total reflectance, exhibits the highest wall heights of 5.5 μm of samples with area less than 30 μm^2. Accordingly, Figure 2.5b shows the wall heights of S1 (3.7 μm), S12 (4.4 μm), and S13 (5.5 μm) corresponding to high total reflectances of 11%, 12%, and 10%, respectively. From the trend shown in Figure 5b, the higher total reflectance of S1 compared with S2–S4 in the UV region cannot be due to a higher wall height. In contrast, in the visible region, the lower total reflectance of S1 than S2–S4 may be due to a lower wall height. Figure 2.5e shows that S12 and S13 have high specular reflectance. This can be explained in that the wall height of highly packed CNTs, formed in cells smaller than 30 μm^2, can serve as glassy carbon of high reflectance, increasing the total and specular reflectance as shown in Fig. 2.9. Hence, it can be concluded that a higher wall height increases the specular and total reflectance for cell areas smaller than 30 μm^2.

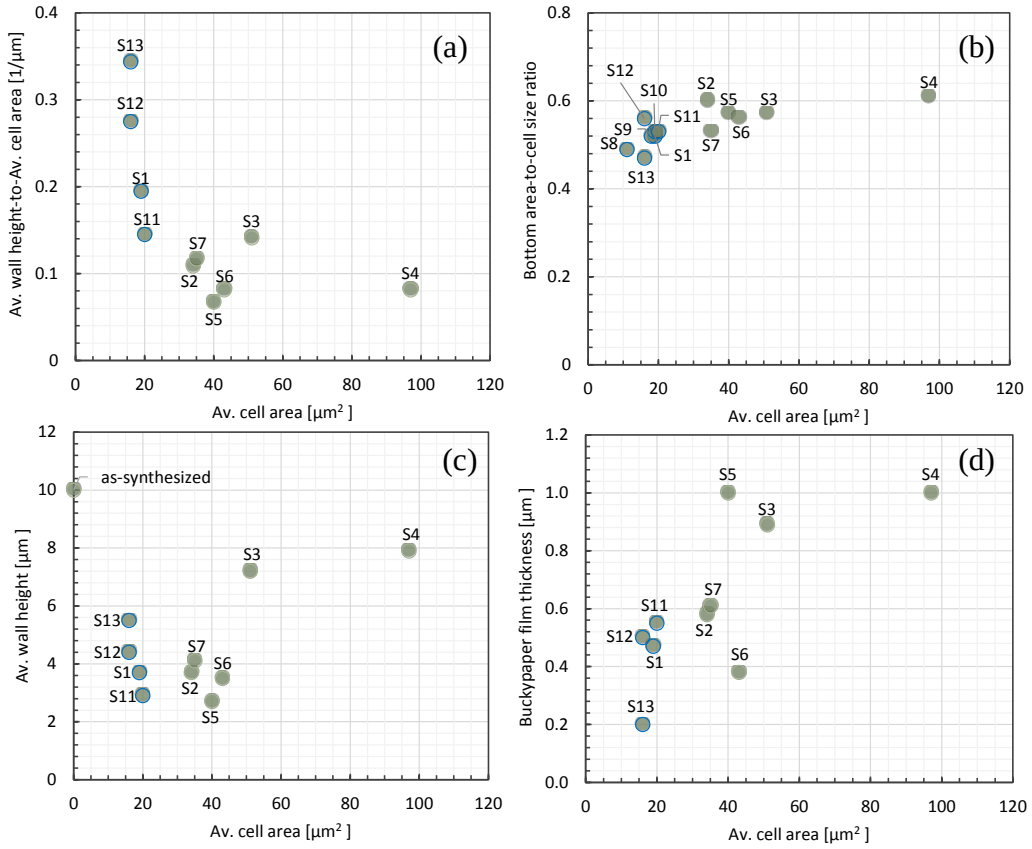

Fig. 2.7 Plots: a) Average wall height to cell area ratio; (b) Bottom area to whole area ratio; (c) Average wall height; and (d) Average buckypaper film thickness as a function of average cell area. Samples with average cell areas of less than 30 μm2 are indicated by green circles with blue outlines. Reprinted from [20].

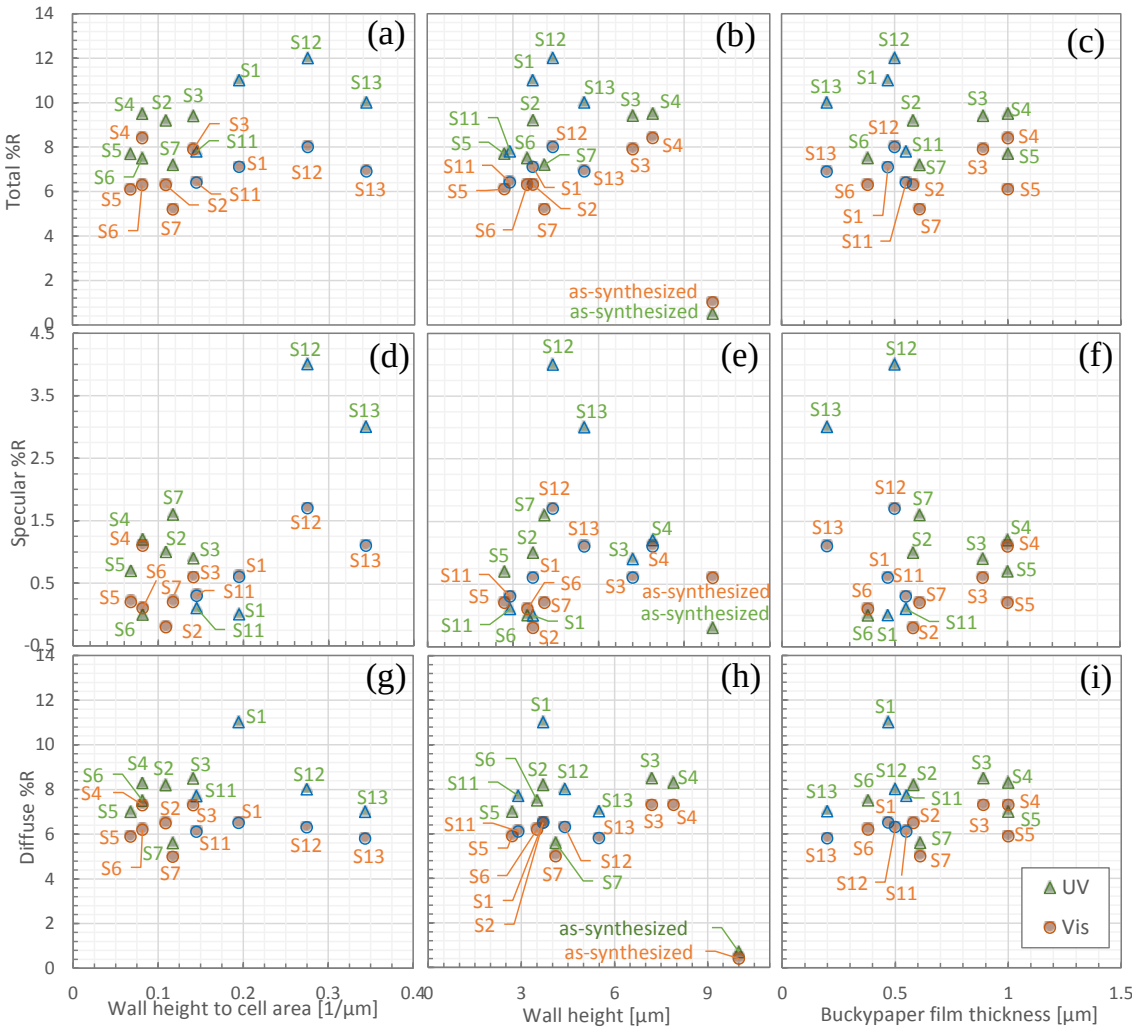

Fig. 2.8 Plots: Total reflectance (Total %R) as a function of (a) Wall height to cell area; (b) Wall height; and (c) Buckypaper film thickness; Specular reflectance (Specular %R) as a function of (d) Wall height to (c) Buckypaper film thickness; Specular reflectance (Specular %R) as a function of (d) Wall height to cell area; (e) Wall height; and (f) Buckypaper film thickness; Diffuse reflectance as a function of (g) cell area; (e) Wall height; and (f) Buckypaper film thickness; Diffuse reflectance as a function of (g) Wall height to cell area; (h) Wall height; and (i) Buckypaper film thickness. UV and visible wavelengths are indicated by green triangles and orange circles, respectively. Samples with a cell area of less than 30 μm^2 are indicated with blue outlines. Reprinted from [20].

Figure 2.7d shows the buckypaper film thickness at the bottom area as a function of cell area. The cell area of 16 μm^2 in S13 gives a thinner buckypaper film thicknesses of 0.20 μm, and the thinner buckypaper film thickness in S13 gives a high total reflectance of 10%, especially in the UV region. Meanwhile films with thicknesses greater than 0.5 μm show a total reflectance lower than 10% in the visible region, as shown in Figure 5c. This result shows a correspondence with

Shabaneh et al.'s findings [23] that the total reflectance of CNT buckypaper films increases with decreased CNT film thicknesses. This behavior can be interpreted as indicating a high reflectance for high-density, thinner-thickness CNT films because the penetration depth of the evanescent field is expected to be small for high-density CNT films. Moreover, Figure 2.8f shows that S12 and S13 have high specular reflectance with thinner buckypaper films. Therefore, thinner buckypaper films can increase the total and specular reflectance. The high total reflectance of S1 compared with S2–S4 in the UV region can be explained as being due to thinner buckypaper films. The total reflectance of S1 is lower as compared with S2–S4 in the visible region is caused by thicker buckypaper films

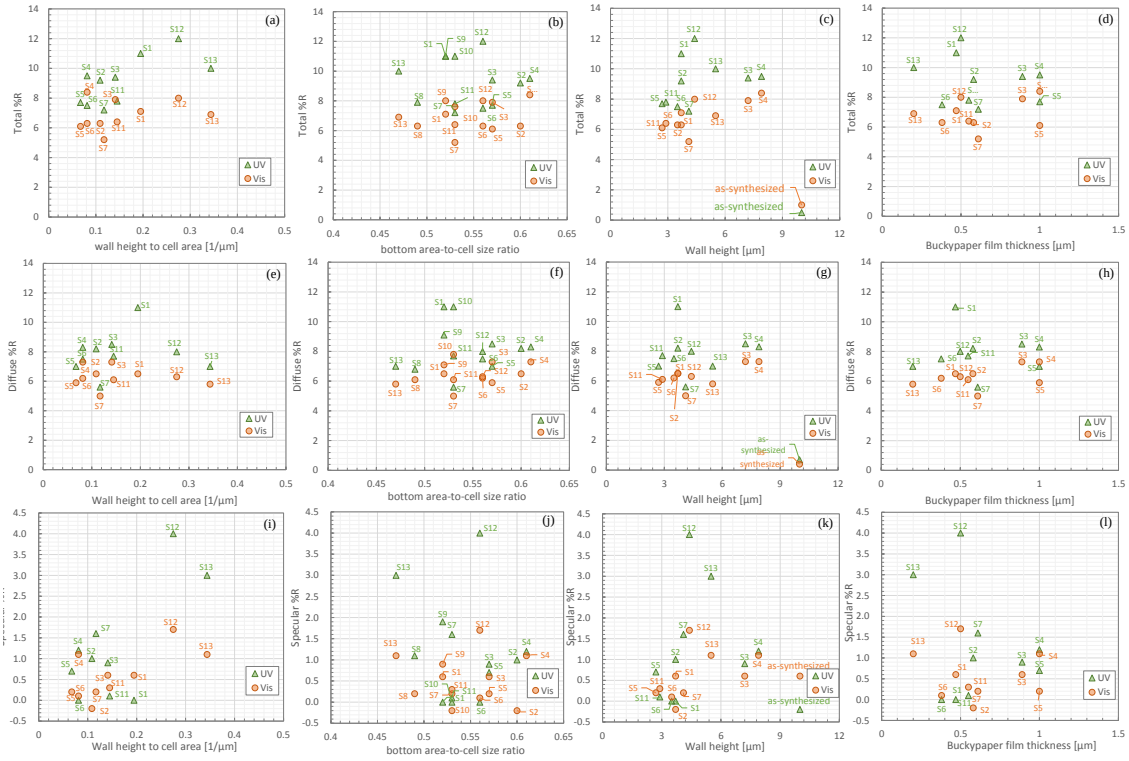

Fig. 2.9 Total, diffuse, specular reflectances vs. CNT honeycomb physical structures. Plots of total (a–d), diffuse (e–h) and specular (i–l) reflectance vs. physical properties of CNT honeycomb: wall height to cell area ratio, bottom to cell size ratio, wall height, and buckypaper film thickness. Reprinted from [20].

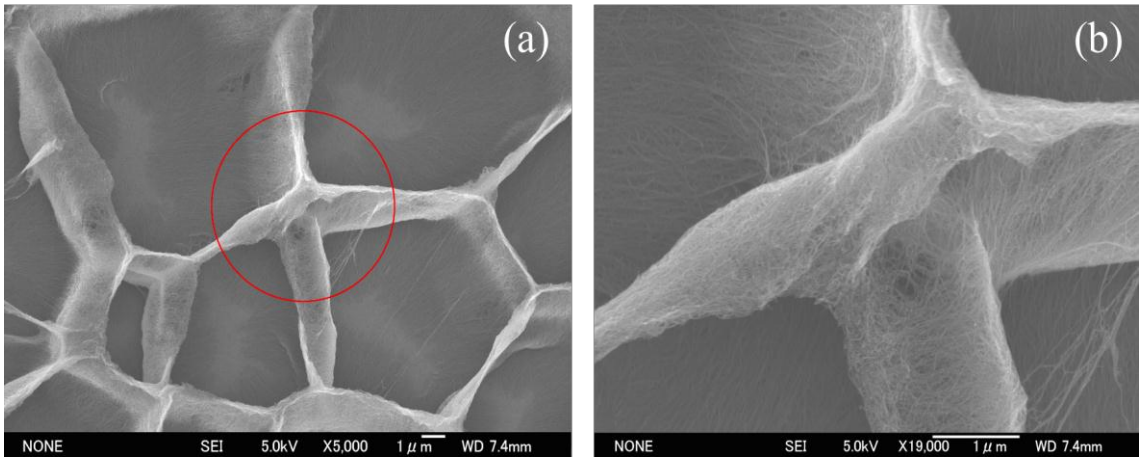

Fig. 2.10 Field-emission scanning electron microscope (FE-SEM) of CNT honeycomb walls. FE-SEM images of (a) CNT honeycomb walls and (b) magnified CNT honeycomb walls. Reprinted from [20].

2.4 Conclusion

This chapter investigated the controlling of cell area in a CNT honeycomb structure by a simple method of ethanol treatment, in which the average cell area could be decreased by a shorter evaporation time of ethanol. The total, diffuse, and specular reflectance of CNT honeycomb structures was investigated. Cell areas smaller than 30 μm^2 with a 3–8 μm wall height showed a higher total reflectance of 6%–12% in the UV region and 6%–8% in the visible region, where as-synthesized CNT forests exhibited corresponding values of 0.5% and 1.0% in the UV and visible regions, respectively. In particular, our findings highlighted that thinner buckypaper films of high-density CNTs in cooperation with a higher ratio of wall height to cell area (larger surface area) and wall height increases the total and specular reflectance. In addition, we found that the highest measured diffuse reflectance of 11% in the UV region, as well as the total reflectance, is likely strongly influenced by a higher total area of buckypapers in CNT walls and bottom areas. Interestingly, this chapter found that the main component of total reflectance from CNT honeycomb structures is diffuse reflectance. It is expected that a higher total reflectance will be obtained for larger surface areas, which will contribute to the achievement of efficient absorption of light into quantum dots to improve the efficiency of QD solar cells utilizing CNT electrodes.

REFERENCES

[1] S. Iijima, “Helical microtubules of graphitic carbon,” *Nature*, vol. 354, no. 6348, pp. 56–58, Nov. 1991.

[2] P. Avouris, M. Freitag, and V. Perebeinos, “Carbon-nanotube photonics and optoelectronics,” *Nature Photonics*, vol. 2, no. 6. pp. 341–350, 2008.

[3] Z. K. Tang *et al.*, “Superconductivity in 4 Angstrom Single-Walled Carbon Nanotubes,” *Science (80-.).*, vol. 292, no. 5526, pp. 2462–2465, 2001.

[4] D. a Walters *et al.*, “Elastic strain of freely suspended single-wall carbon nanotube ropes,” *Appl. Phys. Lett.*, vol. 74, no. 25, pp. 3803–3805, 1999.

[5] K. Cui, T. Chiba, S. Omiya, T. Thurakitseree, P. Zhao, and S. Fujii, “Self-Assembled Microhoneycomb Network of Single-Walled Carbon Nanotubes for Solar Cells,” 2013.

[6] K. Song *et al.*, “Structural polymer-based carbon nanotube composite fibers: Understanding the processing-structure-performance relationship,” *Materials (Basel).*, vol. 6, no. 6, pp. 2543–2577, 2013.

[7] X. Lim, H. W. Gary Foo, G. H. Chia, and C. H. Sow, “Capillarity-assisted assembly of carbon nanotube microstructures with organized initiations,” in *ACS Nano*, 2010, vol. 4, no. 2, pp. 1067–1075.

[8] N. Chakrapani, B. Wei, A. Carrillo, P. M. Ajayan, and R. S. Kane, “Capillarity-driven assembly of two-dimensional cellular carbon nanotube foams.,” *Proc. Natl. Acad. Sci. U. S. A.*, vol. 101, no. 12, pp. 4009–12, 2004.

[9] M. De Volder *et al.*, “Diverse 3D microarchitectures made by capillary forming of carbon nanotubes,” *Adv. Mater.*, vol. 22, no. 39, pp. 4384–4389, 2010.

[10] M. De Volder and A. J. Hart, “Engineering Hierarchical Nanostructures by Elastocapillary Self-Assembly,” *Angew. Chemie Int. Ed.*, vol. 52, no. 9, pp. 2412–2425, 2013.

[11] J. Chen *et al.*, “A quantum dot sensitized solar cell based on vertically aligned carbon nanotube templated ZnO arrays,” *Electrochem. commun.*, vol. 12, no. 10, pp. 1432–1435, 2010.

[12] C. Li *et al.*, “Photovoltaic property of a vertically aligned carbon nanotube hexagonal network assembled with CdS quantum dots,” *ACS Appl. Mater. Interfaces*, vol. 5, no. 15, pp. 7400–7404, 2013.

[13] Z.-P. Yang, L. Ci, J. A. Bur, S.-Y. Lin, and P. M. Ajayan, “Experimental observation of an extremely dark material made by a low-density nanotube array.,” *Nano Lett.*, vol. 8, no. 2, pp. 446–51, Feb. 2008.

[14] E. Shi *et al.*, “TiO2-Coated Carbon Nanotube-Silicon Solar Cells with Efficiency of 15%,” *Sci. Rep.*, vol. 2, p. 884, Nov. 2012.

[15] K. Mizuno *et al.*, “A black body absorber from vertically aligned single-walled carbon nanotubes.,” *Proc. Natl. Acad. Sci. U. S. A.*, vol. 106, no. 15, pp. 6044–6047, 2009.

[16] Y. Murakami, E. Einarsson, T. Edamura, and S. Maruyama, “Polarization dependence of the optical absorption of single-walled carbon nanotubes,” *Phys. Rev. Lett.*, vol. 94, no. 8, pp. 1–4, 2005.

[17] J. Y. Lee *et al.*, “Simple approach for enhancement of light harvesting efficiency of dye-sensitized solar cells by polymeric mirror.,” *Opt. Express*, vol. 18 Suppl 4, no. November, pp. A522–A527, 2010.

[18] H. Koji, H. Furuta, K. Sekiya, N. Nitta, T. Harigai, and A. Hatta, “Increased {CNT} growth density with an additional thin Ni layer on the Fe/Al catalyst film,” *Diam. Relat. Mater.*, vol. 36, no. 0, pp. 1–7, 2013.

[19] C. A. Schneider, W. S. Rasband, and K. W. Eliceiri, “NIH Image to ImageJ: 25 years of image

analysis," *Nat Meth*, vol. 9, no. 7, pp. 671–675, Jul. 2012.
[20] J. Udorn, A. Hatta, and H. Furuta, "Carbon Nanotube (CNT) Honeycomb Cell Area-Dependent Optical Reflectance," *Nanomaterials*, vol. 6, no. 11, p. 202, Nov. 2016.
[21] M. Peters, C. Ulbrich, J. C. Goldschmidt, J. Fernandez, G. Siefer, and B. Bläsi, "Directionally selective light trapping in a germanium solar cell," *Opt. Express*, vol. 19, no. S2, pp. A136–A145, 2011.
[22] M. A. Green and M. J. Keevers, "Optical properties of intrinsic silicon at 300 K," *Prog. Photovoltaics Res. Appl.*, vol. 3, no. 3, pp. 189–192, 1995.
[23] A. A. Shabaneh *et al.*, "Reflectance response of tapered optical fiber coated with graphene oxide nanostructured thin film for aqueous ethanol sensing," *Opt. Commun.*, vol. 331, pp. 320–324, 2014.

CHAPTER 3

CdSe/ZnS quantum dot (QD) sensitized solar cell utilizing a multi-walled carbon nanotube photoanode on a stainless-steel substrate

Abstract: Multi-walled carbon nanotube (MWCNT) forests grown on a stainless-steel substrate were used as a photoanode in CdSe/ZnS (core/shell) quantum dot (QD) sensitized solar cells (QDSSCs). QD-treated MWCNTs on the conductive metal stainless substrate showed a higher power conversion efficiency (PCE) of 0.015% than those grown on a doped silicon substrate with a PCE of 0.005% under AM 1.5 sunlight intensity (100 mW/cm^2). This higher efficiency can be attributed to the lower sheet resistance of 0.0045 Ω/sq for the metal substrate than the value of 259 Ω/sq for doped silicon. The relationship between the total reflectance of the as-prepared CNT photoanode and the PCE was investigated for CNTs of various heights and amounts of QDs. A QDSSC fabricated using a CNT photo anode with a height of 25 μm showed the highest efficiency of 0.014 with the lowest total reflectance of 1.9%, which indicates a higher surface area of CNTs and a larger amount of QDs. The as-grown 25-μm CNTs combined with 25 mL of QDs in toluene solutions exhibited the highest PCE of 0.015%, due to the larger surface area of the CNTs and the higher light absorption from the large amount of QDs on the CNTs.

Keywords: Multi-walled carbon nanotubes (MWCNTs), Quantum dots (QDs), Quantum dot sensitized solar cells (QDSSCs), Power conversion efficiency (PCE)

3.1 Research background and literature review

The extraordinary mechanical, chemical, and electronic properties of carbon nanotubes (CNTs) make them outstanding materials for energy applications [1]–[3]. A major challenge in solar cell applications is the development of modified CNT structures for use as transparent electrodes [4]. The modified CNT structure is expected to be a good material for

use as a counter electrode or photo-anode [4] with semiconducting quantum dots (QDs) in order to harvest a broader range of light from the ultraviolet (UV) to the infrared (IR) [5]. We have reported a significant increase in optical total reflectance using a structural modification of CNT honeycombs [6], which will increase the utility of CNT honeycomb structures in high-efficiency solar cells. QD-decorated CNTs exhibit efficient charge transfer from photo-excited QDs to the CNTs [7]. QD sensitized solar cells (QDSSCs) have attracted considerable interest from researchers because their power conversion efficiency (PCE) may exceed the Shockley and Queisser limits [8], [9]. In particular, QDs can harvest a broad range of optical wavelengths by multiple exciton generation (MEG), thus improving the photovoltaic efficiency [10]–[12]. Optical absorption by QDs fabricated from materials such as CdS [13], CdSe [14], and CdSe/ZnS [15] is intrinsically tunable from the UV to the near-IR due to the particle-size dependence of the bandgap. A major advantage of QDs as light sensitizers compared with conventional dyes is that electron recombination is suppressed, thereby improving the efficiency of QDSSCs [16]–[18]. One dimensional (1D) wires, of e.g., TiO_2 [19], [20], ZnO [21], [22], and Si [23], [24] have been extensively used for electron transfer from QDs to electrodes. In particular, CNTs have arisen as a superior candidate 1D wire electrode material for QDSSC [2], [25], [26] because of their large surface area, high conductivity, high aspect ratio, and chemical stability. Due to their excellent electrical and thermal conductivity, flexible metal substrates serving as a counterelectrode of DSSCs can reduce both the sheet resistance and production cost of solar cells [27]–[29]. It was reported the PCE of QDs/Si coaxial nanowires on the gold (Au) sputtering metal electrode in QDSSCs shows 0.253% [30]. To the best of our knowledge, there are no reports of QDSSCs in which QD-treated CNT forest photoanodes are fabricated on a metal substrate. In this chapter, CNT forests grown on stainless steel serving as a photoanode for CdSe/ZnS core/shell QDSSCs are investigated as a means of improving photovoltaic efficiency. The efficiency was compared for samples of QDSSCs on a metal stainless steel substrate, QDSSCs on a doped silicon substrate, and QDSSCs with a photoanode of randomly oriented CNT (buckypaper) films on a metal stainless steel substrate. The relationship between the optical total reflectance of as-grown CNTs and the PCE, and the impact of the CNT height and QD quantity on the PCE were investigated.

3.2 Material and methods

Vertically aligned multiwalled carbon nanotube (MWCNT) forests with tube diameters of 30–65 nm and heights of ~15 μm were prepared by a catalytic thermal chemical vapour deposition (CVD) method with an annealing time of 2.5 min in a hydrogen flow of 65 sccm at 28 Pa and 730°C, followed by CNT synthesis at 730°C with a carbon source gas of acetylene (C_2H_2) gas at 54 Pa for 10 min on Fe/Al (5/50 nm in thickness) bi-layered catalyst films on a sheet of stainless steel SUS304 (68% iron, 19% chromium, 10% manganese, 1% silicon, and 2% other compounds). The Fe/Al catalyst films on the stainless-steel sheet were deposited by magnetron sputtering under an argon flow of 10 sccm, a pressure of 0.8 Pa, and a discharge current of 40 mA for 21 min for Al and 2.5 min for Fe. CNT buckypaper films were prepared by dipping vertically aligned CNTs grown on the stainless-steel sheet into a methanol solution for 5 min, and then drying them in air at room temperature. The morphologies and heights of the as-grown CNT forests and modified CNT structures were characterized using field-emission scanning electron microscopy (FE-SEM; JEOL JSM-5310). The total reflectance in the UV–vis region was measured using a spectrophotometer (HITACHI U-3900). The photoluminescence spectra were measured using iHR320 Micro-Pl/Raman spectroscope (Horiba) with a 325-nm wavelength of He-Cd laser source in a power of 1 mW. Solar cells were fabricated from as-grown CNT forests and CNT buckypaper films as photoanodes, treated with CdSe/ZnS (core/shell) quantum dots in toluene solutions as a sensitizer with a particle size of 3.4 nm (Lumidot^{TM}, Aldrich). Indium tin oxide (ITO) glass with a sheet resistance of ~15 Ω/sq was used as a counter electrode, and the 0.1-μm^2 active area between the two electrodes was filled with an iodide electrolyte solution (I_1^-/I_3^-). The J–V characteristics of the cells were recorded with a computer-controlled digital source meter (Keithley Model 2400) by applying an external potential bias to the cell under AM 1.5 sunlight intensity (100 mW/cm^2). All measurement was carried out at the room temperature.

3.3 Results and discussions

Figures 1(a – c) show top-view SEM micrographs of as-grown CNTs on a silicon substrate, a stainless-steel substrate, and CNT buckypaper films on a stainless-steel substrate, respectively. The insets show cross-sectional SEM images of each sample. In Fig. 1(b), the

as-grown CNTs on the stainless steel have a variable height from 10 to 25 μm, whereas the as-grown CNTs on the silicon substrate in Fig. 1(a) have a higher density and a uniform height.

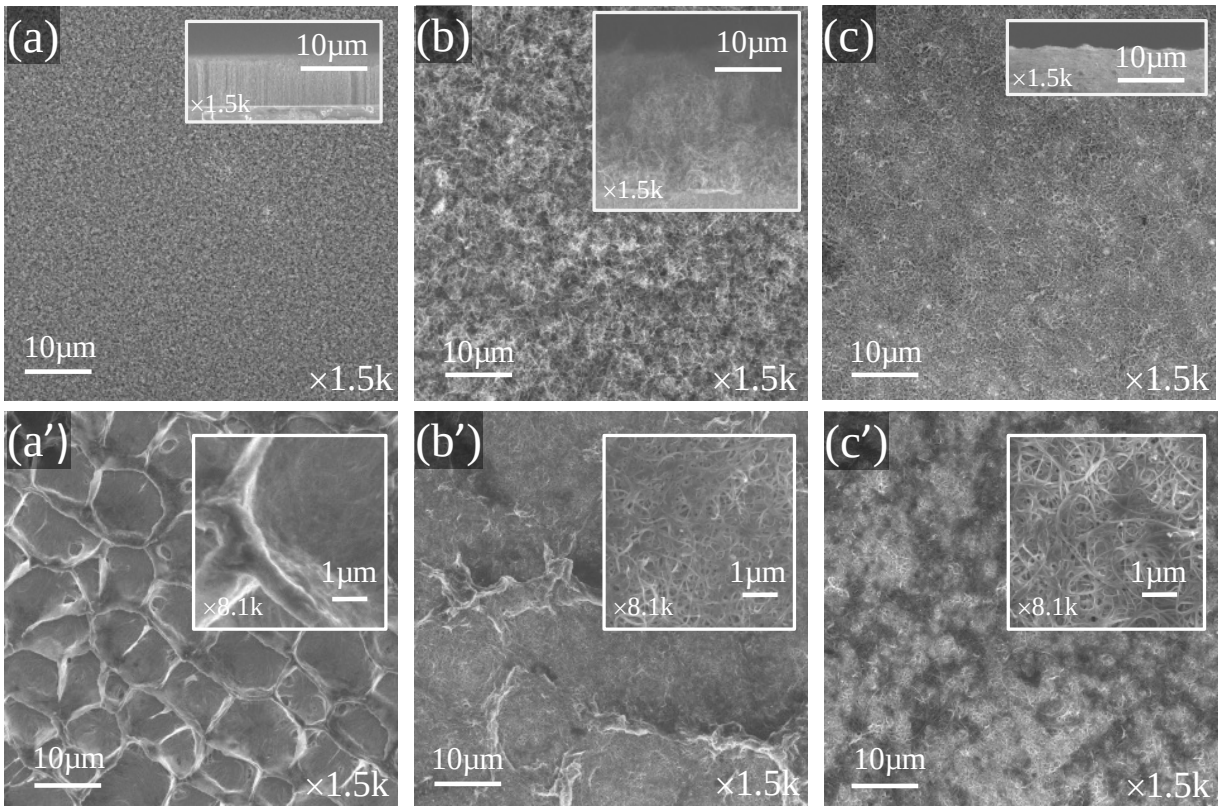

Fig. 3.1 Top-view FE-SEM images of (a) as-grown CNTs on silicon substrate, (b) as-grown CNTs on stainless steel substrate, (c) CNT buckypaper films on stainless steel substrate. The insets show cross-sectional images. CdSe/ZnS QDs-treated on (a') as-grown CNTs on silicon substrate, (b') as-grown CNTs on stainless steel substrate, (c') CNT buckpaper films on stainless steel substrate. The insets show high-magnification images. White and black bars stand for 10 and 1 μm, respectively. Reprinted from [31].

The CNT buckypaper films have highly packed CNTs, as shown in the inset of Fig. 1(c). Figures 1(a' - c') show SEM images after soaking for 1.5 min in 20 μL of QDs in toluene solutions for samples of CNT forests on Si, stainless steel, and buckypaper on stainless steel, respectively. After QD treatment, highly-packed CNT films were formed on the stainless steel, as shown in the inset of Fig. 1(b'), whereas a honeycomb-like CNT structure was formed on the silicon substrate, as shown in Fig. 1(a').

Table 3.1 Properties of QD-treated CNTs on a silicon substrate, and CNT buckypaper films on the stainless-steel substrate, and QDs-treated CNTs on the stainless steel with various heights [31].

	Sheet resistance (Ω/sq)	**Series resistance (Ω/sq)**	**Total reflectance at 560 nm (without QDs)**	**J_{SC} (mA/cm^2)**	**V_{OC} (V)**	**FF**	**η (PCE)**
QD-treated CNTs on silicon substrate	259	33K	0.98%	0.067	0.21	38.6%	0.005%
QD-treated CNT buckypaper films on SUS	0.0046	14 K	4.3%	0.068	0.32	42.9%	0.009%
QD-treated 17-μm CNTs on SUS	0.0047	13K	4.1%	0.050	0.38	56.7%	0.011%
QD-treated 25-μm CNTs on SUS	0.0045	13K	1.9%	0.057	0.45	52.2%	0.014%
QD-treated 33-μm CNTs on SUS	0.0043	14K	2.2%	0.049	0.40	65.6%	0.013%
QD-treated 41-μm CNTs on SUS	0.0043	13K	2.2%	0.056	0.39	54.4%	0.012%

Table 1 shows the sheet resistance, series resistance, optical total reflectance, and PCE for these samples [31], [32]. As-grown CNTs with a height of 25 μm on a stainless-steel substrate with a sheet resistance of 0.0045 Ω/sq and an optical total reflectance of 1.9% at 560 nm exhibit the highest PCE of 0.014%. Meanwhile, as-grown CNTs on a silicon substrate with a higher sheet resistance of 259 Ω/sq exhibit a PCE of 0.005%. The 2.8 times higher PCE for the former sample can be attributed to the higher conductance of the substrate. The PCE for QD-treated CNTs on the stainless-steel substrate is 1.6 times higher than that for CNT buckypaper films on the same metal stainless steel substrate, which can be attributed to the higher number of QDs adsorbed on the surface of the CNTs. QD-treated CNTs on the stainless-steel substrate had heights of 17, 25, 33 and 41 μm, and the PCE was the highest, at 0.014%, for a height of 25 μm. For the taller CNTs, the lower PCE could be explained by the fact that the electron transport path was longer than the electron diffusion

length, leading to increased recombination of electrons and holes [33], and hence a lower efficiency.

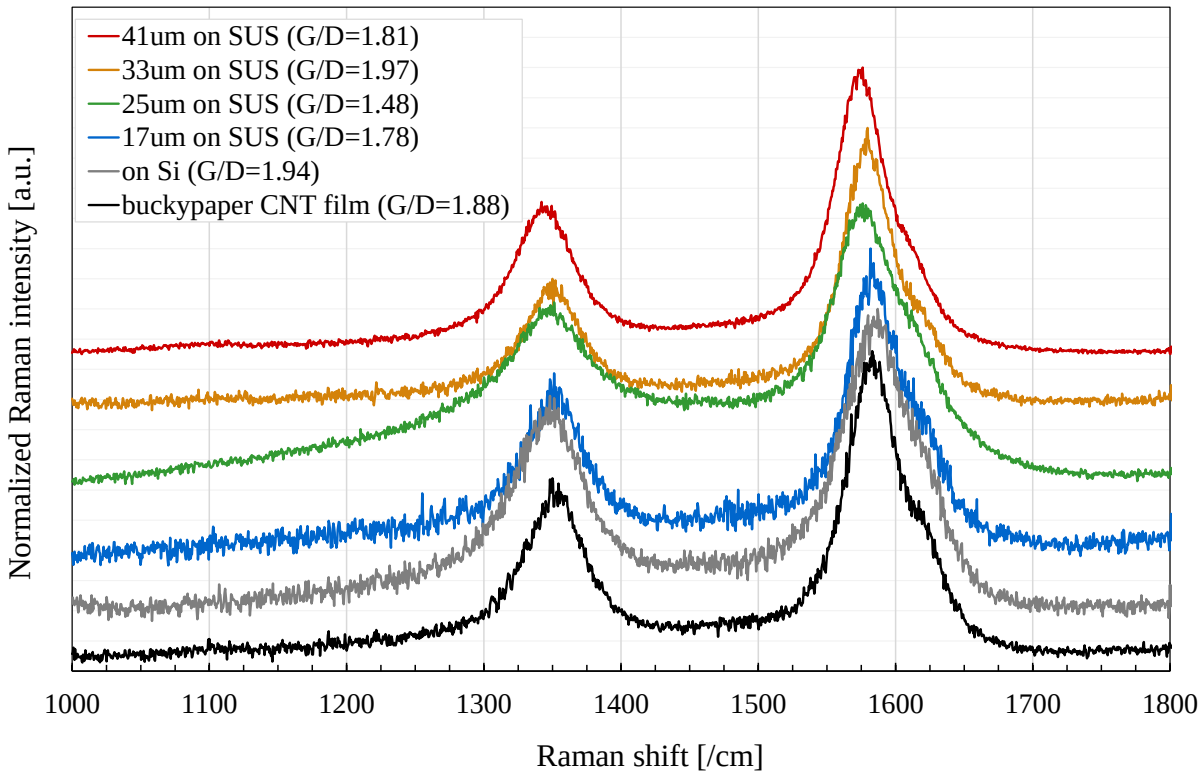

Fig. 3.2 Raman spectra of as-grown CNTs on silicon substrate, CNT buckypaper films on stainless steel substrate, and as-grown CNTs with various heights on stainless steel substrate. The Raman laser wavelength was 532.8 nm. Reprinted from [31].

Figure 2 shows Raman spectra of as-grown CNTs on a silicon substrate, a CNT buckypaper film, and as-grown CNTs of various heights on the stainless-steel substrate. The Raman spectra of all the samples show characteristic D- and G-bands at around 1350 and 1580 cm^{-1}, respectively. The G/D intensity ratio indicates the amount of disorder of the CNTs and graphite crystal [34]. The G/D ratio for as-grown CNTs is 1.48–1.97, and for CNT buckypaper films on a stainless-steel substrate is 1.88, which is lower than the value of 1.94 for as-grown CNTs on a silicon substrate. The G/D ratios for as-grown CNTs with heights of 33 and 41 μm are 1.97 and 1.81, respectively, indicating that a higher number of layers exist in the thicker MWCNT samples on the metal substrates compared with the thinner 17-and 25-μm height CNTs.

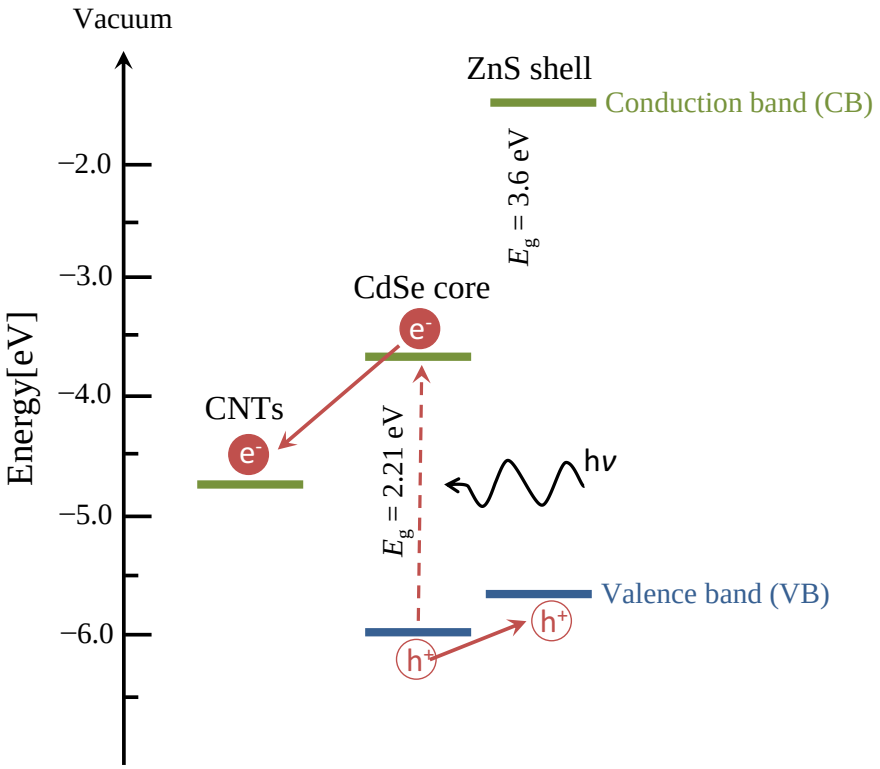

Fig. 3.3 Structure schematic and energy band diagram of CdSe/ZnS (core/shell) QD-treated CNTs on a metal substrate as the photoanode. Reprinted from [31].

Figure 3 shows a schematic energy-level diagram for CNTs and CdSe/ZnS core/shell quantum dots on a metal substrate (modified from[30] [35], [36]). The excitonic transition of CdSe/ZnS corresponds to the size of the QDs of 3.4 nm and the bandgap is 2.21 eV for the wavelength of 561 nm. Exciton of electron hole pair are generated with absorption of light in CdSe core. The electron generated in the conduction band of the CdSe core transfers to the CNT and is collected on the conductive photoanode. Multi-electron generation (MEG) is also possible, generating two or more electron–hole pairs if the photon energy is greater than or equal to 2Eg for CdSe/ZnS (4.42 eV) at 280 nm in the UV region [37].

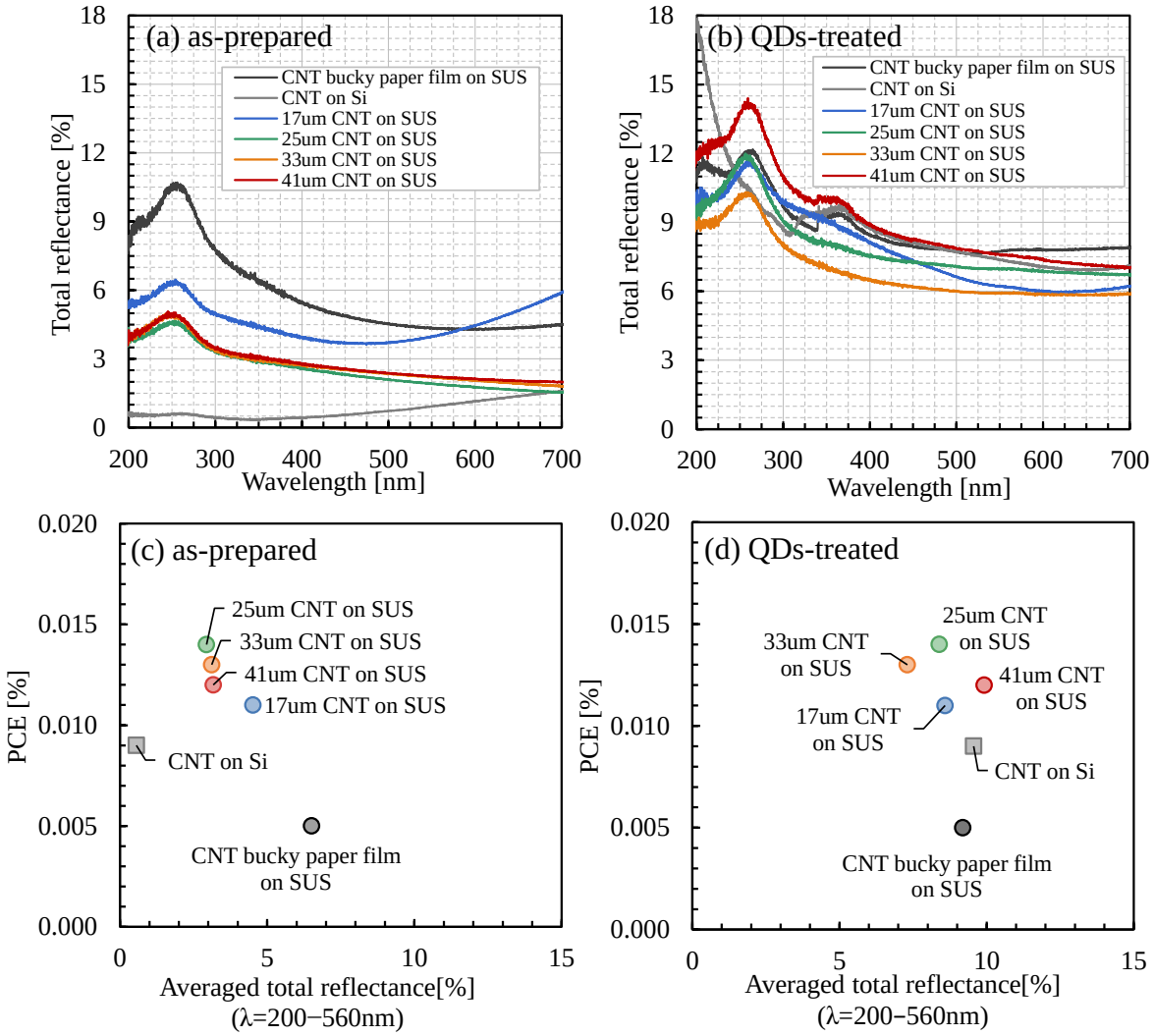

Fig. 3.4 Optical total reflectance of (a) as-prepared and (b) QDs-treated CNTs on silicon substrate (grey), CNT buckypaper films on stainless steel substrate (black), as-prepared CNTs with various heights on stainless steel substrate. PCE vs. optical total reflectance of (c) as-prepared and (d) QDs-treated CNTs. Reprinted from [31].

Figure 4(a) shows the total reflectance of as-grown CNTs on a silicon substrate, a CNT buckypaper film on a stainless-steel substrate, and as-grown CNTs of various heights on a stainless-steel substrate. For as-grown CNTs on the stainless steel before QD treatment, the strong reflection at wavelengths shorter than 380 nm can be assigned to Rayleigh scattering, which provides a higher reflectance at shorter wavelength [38]. The bandgap of CdSe (Eg = 2.21 eV) is corresponded to 561 nm which is expected as an absorption edge of QDs. The CNT buckypaper films (black line) exhibit a higher total reflectance of more than 5% at 200–561 nm due to the highly packed CNTs serving as glassy carbon to strongly reflect light [39].

As-grown CNTs on a silicon substrate (grey line) exhibit the lowest total reflectance of less than 2%, which can be attributed to the higher density of CNT forests. The CNT forest with a height of 25 μm has a lower averaged total reflectance of 2.9% at a wavelength of 200 – 560 nm. This can be explained that multiple scattering of the incident light into the bottom of the CNT forest, so-called blackbody absorption [40] causes the lower total reflectance. Additionally and theoretically, the light incidence on a top surface of CNT forests with a small angle to the CNT axis in which electrons on the CNT body cannot couple with electric fields providing a low optical interaction between the CNT forests and normally incident, resulting the low total reflectance [41]. Figure 4(c) shows the relationship between the total reflectance and the PCE, which indicates that the lower total reflectance of the as-grown CNTs on the stainless steel gives a higher solar cell efficiency after QDSSC fabrication. Significantly, the PCE for QDSSCs with CNTs with heights of 25 μm on a stainless-steel substrate, with the averaged total reflectance of 2.9% (green symbols), has a maximum value of 0.014%. Also, as can be seen in Fig. 4(d), the lower total reflectance of 25 and 33 μm exhibits the better PCE. The lower total reflectance due to efficient absorption of light in CNTs leads to higher solar cell efficiency. The low total reflectance of CNT forests, by the mechanism of the repeated reflection of incident light into the CNT bottom region, indicates a higher CNT surface area, which is expected to adsorb a larger number of QDs generate and transfer electrons into CNTs for the efficient photoconversion resulting in a higher PCE [42].

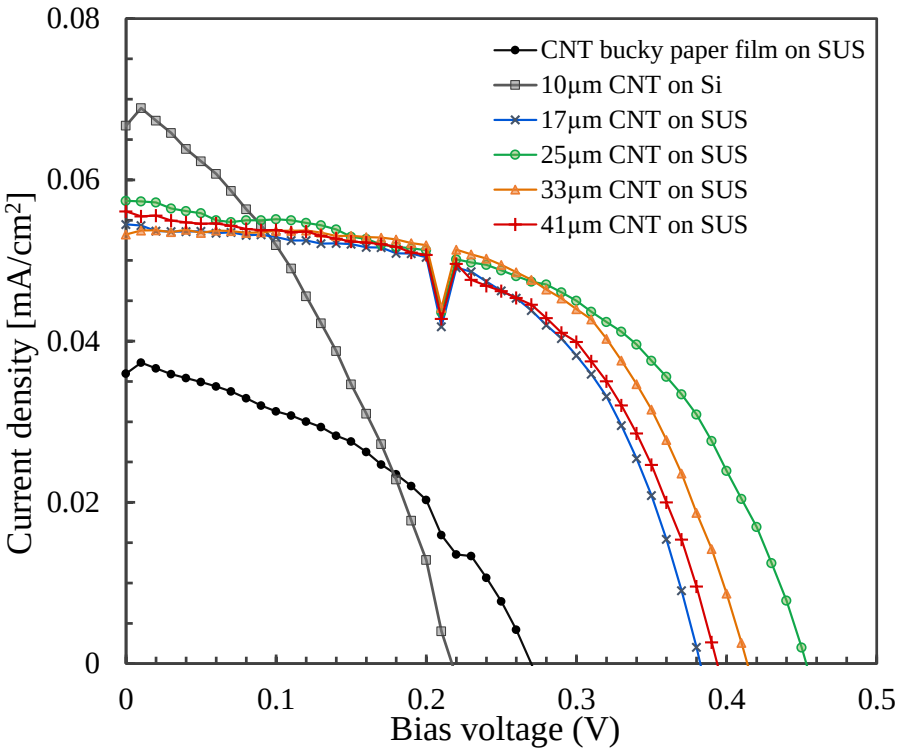

Fig. 3.5: J–V curves of photovoltaic QDSSCs cells of QD-treated CNTs on silicon substrate, CNT buckypaper films on stainless steel substrate, QDs-treated CNTs with various heights on stainless steel substrate. Reprinted from [31].

Figure 5 presents J–V curves for QDSSC cells of QD-treated CNTs on a silicon substrate, QD-treated CNT buckypaper films on a stainless-steel substrate, and QD-treated CNTs with various heights on a stainless-steel substrate. The PCE (η) was calculated using the equation $\eta = (FF \times J_{SC} \times V_{OC}) / P_{input}$, where FF is the fill factor and P_{input} is the power density of the incident light. It can be seen that QD-treated CNTs with a height of 25-μm exhibit significantly better photovoltaic performance in terms of the current density (J_{SC}) and the open-circuit voltage (V_{OC}). Compared to those on the low-conductivity silicon substrate, as-grown CNTs after QD treatment on the stainless-steel substrate also exhibit an improved open-circuit voltage of 0.21 to 0.45 volts (see Table 1). This is evidence that the low resistivity of the conductive substrate, which shows excellent electrical and thermal conductance to enhance electron transport and inhibit electron recombination [28], gives an increased open-circuit voltage, leading to improved solar cell efficiency. The QD-treated CNTs with heights of 25 μm exhibit a higher V_{OC} of 0.45 volts and also slightly improves the V_{OC} from 0.32 to 0.45 volts as compared with CNT buckypaper films. In addition, the energy barrier at the QDSSC/CNT interface can suppress interfacial

recombination [28], [43], leading to an increased V_{OC}, which is expected for CNT forests directly grown on metal substrates. The increase in the PCE is an indication of improved charge collection and transport due to introducing the CNTs forest directly grown on the metal substrate at a significant specific height as an electrode scaffold in the photoanode.

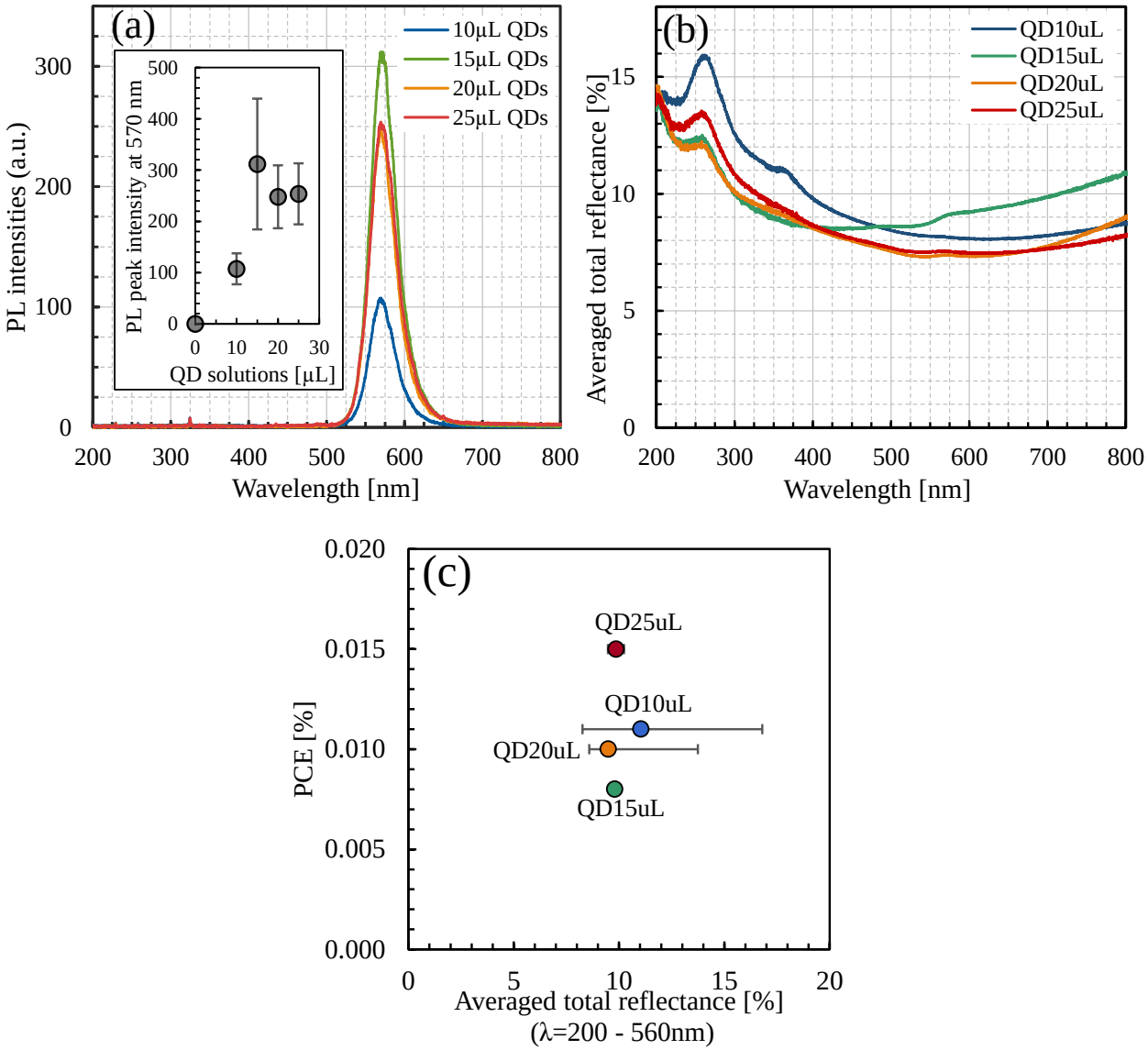

Fig. 3.6 (a) Photoluminescence (PL) spectra of as-grown 25-µm-height CNTs on stainless steel substrate for different amounts of CdSe/ZnS (core/shell) quantum dots of 10, 15, 20, and 25 µl. The excited laser wavelength was 351 nm. Inset: PL peak intensities vs. QD solutions. (b) Total reflectance for varied QDs solutions. (c) PCE vs. averaged total reflectance from 200 – 560 nm. Reprinted from [31].

The amount of QDs in toluene solutions was varied to examine the influence on the PCE. Figure 6(a) shows the photoluminescence (PL) intensities for as-grown CNTs with heights of 25 μm on a stainless-steel substrate for varied amounts of QD solutions. As shown in Fig. 6(a), clear PL peaks for QD-treated CNT forests are found at 570 nm, which corresponds to the bandgap of 2.21 eV (561nm). Comparing the different amount of QDs, it is seen that the highest peak intensity is for 15 μL of QDs, and the largest amount of QDs at 25 μL yields the second highest peak intensity. This can be explained the variation of PL peak intensities caused by the thickness distribution was observed, which are shown in the inset of Fig. 6(a) as error bars. However, an inset of Fig. 6(a) shows a tendency of a dependence of QD solutions and PL peak intensities at 570 nm. In particular, the PCE for a CNT photoanode with 25-μL QD treatment and 7.2% total reflectance has a maximum value of 0.015% (see Table 2). This confirms that a lower total reflectance (higher absorption) contributes to efficient absorption by QDs to increase charge collection for the photoanode leading to improved solar cell efficiencies.

Table 3.2 Properties of as-grown CNTs after QD solution treatment on the stainless-steel substrate for varied amounts of QDs [31].

	Total reflectance at 560 nm (with QDs)	J_{SC} **(mA/cm^2)**	V_{OC} ***(V)***	***FF***	η ***(PCE)***
As-grown CNTs with 10-μl QDs	6.8%	0.058	0.36	51.8%	0.011%
As-grown CNTs with 15-μl QDs	8.9%	0.055	0.29	54.2%	0.008%
As-grown CNTs with 20-μl QDs	7.8%	0.061	0.31	52.1%	0.010%
As-grown CNTs with 25-μl QDs	7.2%	0.058	0.62	41.6%	0.015%

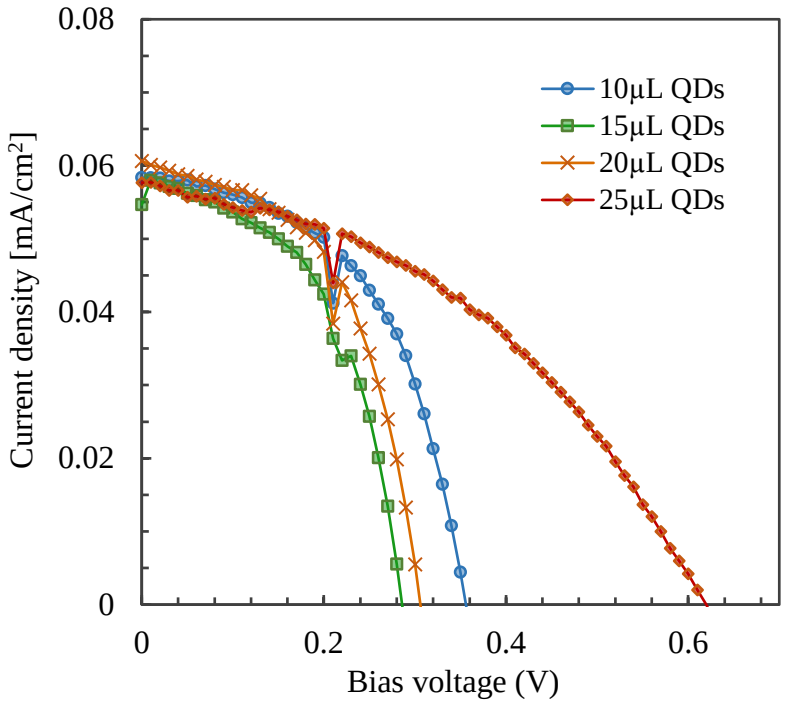

Fig. 3.7: J–V curves of as-grown CNTs on stainless steel substrates for varied amounts of QD solutions. Reprinted from [31].

Figure 7 presents J–V curves for as-grown CNTs on a stainless-steel substrate with varied amounts of QDs. The as-grown CNTs treated with 25 µL of QDs also exhibit an improvement in the open-circuit voltage from 0.36 to 0.62 V compared with 10 µL of QDs (see Table 2). This could be concluded the larger amount of QDs more collect charges for the photoanode resulting to increase the *Voc*. The data shows that the efficiency of as-grown CNTs with 25 µL of QDs is the highest at 0.015%. Thus, larger amounts of QDs lead to improved solar cell efficiency because they can absorb direct incident light and reflected light from CNTs to generate more electron–hole pairs for photoanodes to improve the solar cell efficiency.

3. 4 Conclusion

This chapter reported the first QDSSCs with photoanodes of MWCNTs on a metal substrate, and found that the PCE for such QDSSCs on stainless steel substrates was three times higher than those on a low-resistive (0.15 Ω·cm), doped silicon substrate. A QD-treated MWCNT forest on a metal substrate was found to have a resistance of 0.0045 Ω/sq and exhibited a higher PCE of 0.015%, whereas QD-treated MWCNTs on a doped silicon substrate had a resistance of 259 Ω/sq and a lower efficiency of 0.005%. This difference could be attributed to the fact that the very low sheet resistivity of a metal substrate gives a higher electrical conductance leading to a higher cell efficiency. The relationship between the total reflectance of QD-treated CNT forests and the PCE was investigated. It was shown that the lower total reflectance QD-treated CNT forest of 25-μm height achieved a higher PCE of 0.014%, likely due to the higher light absorption in the QDs. Although the efficiency is currently low compared with that of high-performance DSSCs or QDSSCs, the successful incorporation of QDs with a CNT forest on a conductive substrate as a photoanode for solar cells has been demonstrated for the first time.

REFERENCES

[1] S. Iijima, “Helical microtubules of graphitic carbon,” *Nature*, vol. 354, no. 6348, pp. 56–58, Nov. 1991.

[2] P. Dong *et al.*, “Vertically aligned single-walled carbon nanotubes as low-cost and high electrocatalytic counter electrode for dye-sensitized solar cells.,” *ACS Appl. Mater. Interfaces*, vol. 3, no. 8, pp. 3157–61, 2011.

[3] H. W. Zhu, H. F. Zeng, V. Subramanian, C. Masarapu, K. H. Hung, and B. Q. Wei, “Anthocyanin-sensitized solar cells using carbon nanotube films as counter electrodes,” *Nanotechnology*, vol. 19, no. 46, p. 5, 2008.

[4] K. Cui *et al.*, “Self-assembled microhoneycomb network of single-walled carbon nanotubes for solar cells,” *J. Phys. Chem. Lett.*, vol. 4, no. 15, pp. 2571–2576, 2013.

[5] S. Hickey, D. Riley, and E. Tull, “Photoelectrochemical studies of CdS nanoparticle modified electrodes: Absorption and photocurrent investigations,” *J. Phys. Chem. B*, vol. 104, no. 32, pp. 7623–7626, Jun. 2000.

[6] J. Udorn, A. Hatta, and H. Furuta, “Carbon Nanotube (CNT) Honeycomb Cell Area-Dependent Optical Reflectance,” *Nanomaterials*, vol. 6, no. 11, p. 202, 2016.

[7] J. M. Haremza, M. a. Hahn, T. D. Krauss, S. Chen, and J. Calcines, “Attachment of Single CdSe Nanocrystals to Individual Single-Walled Carbon Nanotubes,” *Nano Lett.*, vol. 2, no. 11, pp. 1253–1258, Nov. 2002.

[8] K. Watanabe *et al.*, “Si/Si 1-xGe x nanopillar superlattice solar cell: A novel nanostructured solar cell for overcoming the Shockley-Queisser limit,” in *Technical Digest - International Electron Devices Meeting, IEDM*, 2011, p. 36.4.1-36.4.4.

[9] O. D. Miller, E. Yablonovitch, and S. R. Kurtz, “Strong internal and external luminescence as solar cells approach the Shockley-Queisser limit,” *IEEE J. Photovoltaics*, vol. 2, no. 3, pp. 303–311, 2012.

[10] P. Péchy *et al.*, “Engineering of Efficient Panchromatic Sensitizers for Nanocrystalline TiO2-Based Solar Cells,” *J. Am. Chem. Soc.*, vol. 123, no. 8, pp. 1613–1624, 2001.

[11] A. V Barve, S. Meesala, S. Sengupta, J. O. Kim, S. Chakrabarti, and S. Krishna, “Effects of contact space charge on the performance of quantum intersubband photodetectors,” *Appl. Phys. Lett.*, vol. 100, no. 19, p. , 2012.

[12] J. D. Mar, X. L. Xu, J. J. Baumberg, A. C. Irvine, C. Stanley, and D. A. Williams, “Voltage-controlled electron tunneling from a single self-assembled quantum dot embedded in a two-dimensional-electron-gas-based photovoltaic cell,” *J. Appl. Phys.*, vol. 110, no. 5, p. , 2011.

[13] K. Yu, G. Lu, K. Chen, S. Mao, H. Kim, and J. Chen, “Controllable photoelectron transfer in CdSe nanocrystal-carbon nanotube hybrid structures,” *Nanoscale*, vol. 4, no. 3, pp. 742–746, 2012.

[14] J. Tian *et al.*, “ZnO/TiO2 nanocable structured photoelectrodes for CdS/CdSe quantum dot co-sensitized solar cells,” *Nanoscale*, vol. 5, no. 3, pp. 936–943, 2013.

[15] S.-W. Baek *et al.*, “Effect of Core Quantum-dots Size on Power-conversion-efficiency for Silicon Solar-cells Implementing Energy-down-shift using CdSe/ZnS Core/Shell Quantum Dots,” *Nanoscale*, Aug. 2014.

[16] E. T. Hoke *et al.*, “The role of electron affi nity in determining whether fullerenes catalyze or inhibit photooxidation of polymers for solar cells,” *Adv. Energy Mater.*, vol. 2, no. 11,

pp. 1351–1357, 2012.

[17] Y. Li, L. Wei, R. Zhang, Y. Chen, and J. Jiao, “Annealing Effect on Photovoltaic Performance of CdSe Quantum-Dots-Sensitized TiO $_2$ Nanorod Solar Cells,” *J. Nanomater.*, vol. 2012, pp. 1–6, 2012.

[18] M. C. Beard, “Multiple exciton generation in semiconductor quantum dots,” *Journal of Physical Chemistry Letters*, vol. 2, no. 11. pp. 1282–1288, 2011.

[19] I. Zarazúa *et al.*, “Photovoltaic conversion enhancement of CdSe quantum dot-sensitized TiO 2 decorated with Au nanoparticles and P3OT,” *J. Phys. Chem. C*, vol. 115, no. 46, pp. 23209–23220, 2011.

[20] N. Guijarro, T. Lana-Villarreal, I. Mora-Ser??, J. Bisquert, and R. G??mez, “CdSe quantum dot-sensitized TiO2 electrodes: Effect of quantum dot coverage and mode of attachment,” *J. Phys. Chem. C*, vol. 113, no. 10, pp. 4208–4214, 2009.

[21] C. Li *et al.*, “Photovoltaic property of a vertically aligned carbon nanotube hexagonal network assembled with CdS quantum dots.,” *ACS Appl. Mater. Interfaces*, vol. 5, no. 15, pp. 7400–4, Aug. 2013.

[22] Y. Zhang *et al.*, “Surface photovoltage characterization of a ZnO nanowire array/CdS quantum dot heterogeneous film and its application for photovoltaic devices,” *Nanotechnology*, vol. 20, no. 15, p. 155707, 2009.

[23] T. Takahashi, “Photoassisted Kelvin probe force microscopy on multicrystalline Si solar cell materials,” in *Japanese Journal of Applied Physics*, 2011, vol. 50, no. 8 PART 4.

[24] R. Jeyakumar, T. K. Maiti, and A. Verma, “Influence of emitter bandgap on interdigitated point contact back heterojunction (a-Si:H/c-Si) solar cell performance,” *Sol. Energy Mater. Sol. Cells*, vol. 109, pp. 199–203, 2013.

[25] F. Malara, M. Manca, L. De Marco, P. Pareo, and G. Gigli, “Flexible carbon nanotube-based composite plates as efficient monolithic counter electrodes for dye solar cells,” *ACS Appl. Mater. Interfaces*, vol. 3, no. 9, pp. 3625–3632, 2011.

[26] T. Peng, P. Zeng, D. Ke, X. Liu, and X. Zhang, “Hydrothermal Preparation of Multiwalled Carbon Nanotubes (MWCNTs)/CdS Nanocomposite and Its Efficient Photocatalytic Hydrogen Production under Visible Light Irradiation,” *Energy & Fuels*, vol. 25, no. 5, pp. 2203–2210, 2011.

[27] M. G. Kang, N.-G. Park, K. S. Ryu, S. H. Chang, and K.-J. Kim, “A 4.2% efficient

flexible dye-sensitized TiO2 solar cells using stainless steel substrate," *Sol. Energy Mater. Sol. Cells*, vol. 90, no. 5, pp. 574–581, Mar. 2006.

[28] K. Miettunen, J. Halme, M. Toivola, and P. Lund, "Initial Performance of Dye Solar Cells on Stainless Steel Substrates," *J. Phys. Chem. C*, vol. 112, no. 10, pp. 4011–4017, 2008.

[29] T. L. Ma, X. M. Fang, M. Akiyama, K. Inoue, H. Noma, and E. Abe, "Properties of several types of novel counter electrodes for dye-sensitized solar cells," *J. Electroanal. Chem.*, vol. 574, no. 1, pp. 77–83, 2004.

[30] Y. Hsieh, M. Lee, and G. Wang, "Sb2S3 Quantum-Dot Sensitized Solar Cells with Silicon Nanowire Photoelectrode," *Int. J. Photoenergy*, vol. 2015, pp. 1–10, 2015.

[31] J. Udorn, S. Hou, C. Li, A. Hatta, and H. Furuta, "CdSe / ZnS Quantum Dot (QD) Sensitized Solar Cell Utilizing a Multi-Walled Carbon Nanotube Photoanode on a Stainless Steel Substrate," vol. 12, 2017. To be published on May 2017

[32] J. Udorn, H. Sachio, S. Hou, C. Li, A. Hatta, and H. Furuta, "CdSe/ZnS (Core/Shell) Quantum Dots Multi-wallled Carbon Nanotubes (MWCNTs) on a Stainless Steel as a Photoanode in Solar Cells," pp. 158–163, 2017.

[33] J. Wei, C. Zhang, Z. Du, H. Li, and W. Zou, "Modification of carbon nanotubes with 4-mercaptobenzoic acid-doped polyaniline for quantum dot sensitized solar cells," *J. Mater. Chem. C*, pp. 4177–4185, 2014.

[34] P. Tan *et al.*, "Comparative Raman Study of Carbon Nanotubes Prepared by D.C. Arc Discharge and Catalytic Methods," *J. Raman Spectrosc.*, vol. 28, no. 5, pp. 369–372, 1997.

[35] L.-H. Lai, W. Gomulya, L. Protesescu, M. V. Kovalenko, and M. A. Loi, "High performance photoelectrochemical hydrogen generation and solar cells with a double type II heterojunction," *Phys. Chem. Chem. Phys.*, vol. 16, no. 16, p. 7531, 2014.

[36] H.-Y. Si, C.-H. Liu, H. Xu, T.-M. Wang, and H.-L. Zhang, "Shell-Controlled Photoluminescence in CdSe/CNT Nanohybrids," *Nanoscale Research Letters*, vol. 4, no. 10. pp. 1146–1152, 2009.

[37] P. V Kamat, "Quantum Dot Solar Cells. Semiconductor Nanocrystals as Light Harvesters," vol. 112, no. October, pp. 18737–18753, 2008.

[38] Z. Yu and and Louis Brus*, "Rayleigh and Raman Scattering from Individual Carbon

Nanotube Bundles," *J. Phys. Chem. B*, vol. 105, no. 6, pp. 1123–1134, 2001.

[39] A. A. Shabaneh *et al.*, "Reflectance Response of Optical Fiber Coated With Carbon Nanotubes for Aqueous Ethanol Sensing," *IEEE Photonics J.*, vol. 6, no. 6, 2014.

[40] K. Mizuno *et al.*, "A black body absorber from vertically aligned single-walled carbon nanotubes.," *Proc. Natl. Acad. Sci. U. S. A.*, vol. 106, no. 15, pp. 6044–6047, 2009.

[41] Y. Murakami, E. Einarsson, T. Edamura, and S. Maruyama, "Polarization dependence of the optical absorption of single-walled carbon nanotubes," *Phys. Rev. Lett.*, vol. 94, no. 8, pp. 1–4, 2005.

[42] I. Robel, B. a. Bunker, and P. V. Kamat, "Single-Walled Carbon Nanotube-CdS Nanocomposites as Light-Harvesting Assemblies: Photoinduced Charge-Transfer Interactions," *Adv. Mater.*, vol. 17, no. 20, pp. 2458–2463, Oct. 2005.

[43] C. V. V. M. Gopi, M. Venkata-Haritha, S.-K. Kim, and H.-J. Kim, "Facile fabrication of highly efficient carbon nanotube thin film replacing CuS counter electrode with enhanced photovoltaic performance in quantum dot-sensitized solar cells," *J. Power Sources*, vol. 311, pp. 111–120, 2016.

CHAPTER 4

OVERALL CONCLUSION

This dissertation focuses on an application of CNTs to improve an efficiency of quantum dot solar cells (QDSSCs) utilizing optical reflectance carbon nanotubes. The originality ideas were provided firstly to utilize the reflected light, total, diffuse, and specular optical reflectance of carbon nanotube (CNT) honeycomb structures. Secondly, the novel study is to investigate efficiencies improvement by the utilization of optical reflectance to improve the quantum dot sensitized solar cell (QDSSCs) efficiency, and to investigate CNT forests grown on stainless steel serving as a photoanode for CdSe/ZnS core/shell QDSSCs as a means of reducing the resistivity to improve photovoltaic efficiency.

4.1 Part I of Research Work

The total, diffuse, and specular reflectance of CNT honeycomb structures was investigated. Cell areas smaller than 30 μm2 with a 3–8 μm wall height showed a higher total reflectance of 6%–12% in the UV region and 6%–8% in the visible region, where as-synthesized CNT forests exhibited corresponding values of 0.5% and 1.0% in the UV and visible regions, respectively. In particular, our findings highlighted that thinner buckypaper films of high-density CNTs in cooperation with a higher ratio of wall height to cell area (larger surface area) and wall height increases the total and specular reflectance. In addition, we found that the highest measured diffuse reflectance of 11% in the UV region, as well as the total reflectance, is likely strongly influenced by a higher total area of buckypapers in CNT walls and bottom areas. Interestingly, this study found that the main component of total reflectance from CNT honeycomb structures is diffuse reflectance. In the next part, it is expected that a total reflectance will be obtained for larger surface areas, which will contribute to the achievement of efficient absorption of light into quantum dots to improve the efficiency of QD solar cells utilizing CNT electrodes.

4.2 Part II of Research Work

Multi-walled carbon nanotube (MWCNT) forests grown on a stainless-steel substrate were used as a photoanode in CdSe/ZnS (core/shell) quantum dot (QD) sensitized solar cells (QDSSCs). QD-treated MWCNTs on the conductive metal stainless substrate showed a higher power conversion efficiency (PCE) of 0.015% than those grown on a doped silicon substrate with a PCE of 0.005% under AM 1.5 sunlight intensity (100 mW/cm^2). This higher efficiency can be attributed to the lower sheet resistance of 0.0045 Ω/sq for the metal substrate than the value of 259 Ω/sq for doped silicon. The relationship between the total reflectance of the as-prepared CNT photoanode and the PCE was investigated for CNTs of various heights and amounts of QDs. A QDSSC fabricated using a CNT photo anode with a height of 25 μm showed the highest efficiency of 0.014% with the lowest total reflectance of 1.9%, which indicates a higher surface area of CNTs and a larger amount of QDs. The as-grown 25-μm CNTs combined with 25 mL of QDs in toluene solutions exhibited the highest PCE of 0.015%, due to the larger surface area of the CNTs and the higher light absorption from the large amount of QDs on the CNTs.

LISTS OF PUBLICATIONS AND CONFERENCES

1. Peered review journals/Proceedings (4)

（1） **J. Udorn**, A. Hatta, H. Furuta, *"Carbon Nanotube (CNT) Honeycomb Cell Area-Dependent Optical Reflectance"*, Nanomaterials. 6 (2016) 202, this journal included in WOS, IF:2.69, Q1 in Material Sciences)

（2） **J. Udorn**, S. Hou, C. Li, A. Hatta, H. Furuta, *"CdSe/ZnS quantum dot (QD) sensitized solar cell utilizing a multi-walled carbon nanotube photoanode on a stainless-steel substrate"*, (Accepted to publish in International Journal of Electrochemical Science, Vol.12, 2017, this journal included in WOS, IF:1.692, Q3),

（3） **J. Udorn**, K. Sekiya, H. Furuta, J. S. Oh and A. Hatta, *"Optical reflectance of deformed MWCNT forests after wettability test"*, published in conference proceedings, TJIA2014 (Thailand-Japan International Academic Conference), (Nov. 2014)

（4） **J. Udorn**, S. Hou, S. Hayashi, C. Li, A. Hatta, H. Furuta, *"CdSe/ZnS (core/Shell) quantum dot (QD) multi-walled carbon nanotubes (MWCNTs) on on a stainless steel as a photoanode in solar cells"*, published in conference proceedings in 5th International Conference on Photonics, Optics and Laser Technology (PHOTOPTICS 2017), (Feb. 2017)

2. International conferences (7)

(1) **J. Udorn**, S. Hou, S. Hayashi, C. Li, A. Hatta, H. Furuta, *"CdSe/ZnS (core/Shell) quantum dot (QD) multi-walled carbon nanotubes (MWCNTs) on on a stainless steel as a photoanode in solar cells"*, PHOTOPTICS2017 (5th International Conference on Photonics, Optics and Laser Technology), (27^{th} Feb. – 1^{st} Mar 2017, Porto, Portugal).

(2) **J. Udorn**, S. Hou, S. Hayashi, C. Li, A. Hatta, H. Furuta, *"Multi-walled carbon nanotubes (MWCNTs) on a metal substrate with quantum dots in*

photovoltaics", MSAT9 (The 9th MATERIAL SCIENCE ACADEMIC THAILAND), (15-16 Dec. 2016, Swissotel Le Concorde, Bangkok, Thailand).

(3) **J. Udorn**, S. Hou, C. Li, A. Hatta, H. Furuta, *"Quantum dots (QDs) mediated dye sensitized solar cells (DSSC) with self-assembled honeycomb photoanode of multi walled carbon nanotube (MWCNT) forests"*, NT-15 (The 15th International Conference on the Science and Applications of Nanotubes), (29th Jun. –3rd Jul. 2015, Nagoya Univ., Nagoya, Japan).

(4) **J. Udorn**, K. Sekiya, H. Furuta, A. Hatta, *"Surface Morphology and Optical Reflectance of Multi-Walled Carbon Nanotube (MWCNT) Forests after Wettability Treatment"*, TMETC8 (The 8th Thailand Metallurgy Conference), (15-16 Dec. 2014, Swissotel Le Concorde, Bangkok, Thailand).

(5) **J. Udorn**, K. Sekiya, H. Furuta, J. -S. Oh and A. Hatta, *"Optical reflectance of deformed MWCNT forests after wettability test"*, TJIA2014 (Thailand-Japan International Academic Conference), (22nd Nov. 2014, U. Tokyo, Tokyo, Japan).

(6) **J. Udorn**, K. Sekiya, H. Furuta, and A. Hatta, *"Optical Properties of Quantum Dots Beaded to Multi-Walled Carbon Nanotube Forest (QD-Beaded MWCNT Forest)"*, FNTG2014 (The 47th Fullerenes-Nanotubes-Graphene General Symposium), (3rd Sep. 2014, Nagoya Univ., Nagoya, Japan).

(7) H. Furuta, K. Sekiya, A. Pander, **J. Udorn**, H. Koji, A. Hatta, K. Takano, and M. Nakajima, *"Optical and THz properties of carbon nanotube forests"*, NT15, (29th Jun. – 2nd Jul. 2013, Nagoya Univ., Nagoya, Japan).

3. Domestic conferences (7)

J. Udorn, S. Hou, C. Li, A. Hatta, H. Furuta,"Carbon nanotube (CNT) honeycomb structure after quantum dot (QD) treatment for solar cells", Nanotech. Symposium 2015, (Nov. 14. 2015, KUT)

4. Best presentation award (1)

J. Udorn, K. Sekiya, H. Furuta, J. -S. Oh and A. Hatta, *"Optical reflectance of deformed MWCNT forests after wettability test"*, TJIA2014 (Thailand-Japan International Academic Conference), (22 Nov. 2014, U. Tokyo, Tokyo, Japan).

5. Publications before enrolling Kochi University of Technology (KUT)

(1) **J. Udorn**, S. Unai, P. Kanthang, W. Ngamsaad, C. Modchang, W. Triampo, C. Krittanai, D. Wtriampo, Y. Lenbury, *Single-particle tracking method for quantitative tracking and biophysical studies of the MinE protein*, J. Korean Phys. Soc. 52 (2008) 639–648. (IF:0.445)

(2) S. Unai, P. Kanthang, **J. Udorn**, W. Ngamsaad, W. Triampo, C. Modchang, C. Krittanai, *Quantitative analysis of time-series fluorescence microscopy using a spot tracking method: application to Min protein dynamics*, Biologia (Bratisl). 64 (2009) 27–42. (IF:0.719)

(3) C. Modchang, W. Triampo, P. Kanthang, **J. Udorn**, S. Unai, W.Ngamsaad, N. Nuttavut, D. Triampo, Y. Lenbury, *Stochastic modeling of external electric field effect on Escherichia coli Min protein dynamics*, J. Korean Phys. Soc. 53 (2008) 851–862. (IF:0.445)

BIOGRAPHY

NAME:	Udorn Janthorn
DATE OF BIRTH:	August 18th, 1982
PLACE OF BIRTH:	Phathang, Huayhaeng, Banrai, Uthaithani, Thailand
INSTITUTION ATTENDED:	1. King Mongkut's University of Technology Thonburi (KMUTT), 2001-2005 Bachelor of Science (Physics) (B.Sc) 2. Mahidol University (MU), 2005-2008 Master of Science (Physics) (M.Sc.) 3. Kochi University of Technology (KUT), 2013-2017, Doctor of Philosophy (Ph.D.) (Electronic and Photonics System Engineering)
STUDY GRANT:	Teaching Assistantships (TA), Thailand Japanese Government Scholarship (MEXT), Japan Special Scholarship Program (SSP) from KUT, Japan
HOME ADDRESS	45 Moo 5, Huayhaeng, Banrai, Uthaithani, Thailand, 61140, Tel. +668-1653-1025
OFFICE ADDRESS	Faculty of Engineering Thai-Nichi Institute of Technology 1771/1, Patanakarn 37, Suanluang Bangkok,Thailand 10250, Tel. +662-7632905
E-MAIL	udorn@tni.ac.th donchanthorn@gmail.com